Advances in Uncertainty Quantification for Computational Electromagnetics

By

Sathya Swaroop Ganta

A dissertation submitted in partial fulfillment of
the requirements for the degree of

Doctor of Philosophy
(Electrical Engineering)

at the
UNIVERSITY OF WISCONSIN–MADISON
2018

Date of final oral examination: 05/23/2018

The dissertation is approved by the following members of the Final Oral Committee:
Susan C. Hagness, Professor, Electrical and Computer Engineering
Barry Vanveen, Professor, Electrical and Computer Engineering
John A. Gubner, Professor, Electrical and Computer Engineering
Benjamin Peherstorfer, Assistant Professor, Mechanical Engineering

ACKNOWLEDGMENTS

I thank my advisors, Prof. Susan C. Hagness and Prof. Barry D. Van Veen, for guiding and motivating me. I thank Dr. Timothy J. Colgan for his research work that formed the basis for my second research aim. I thank Dr. Owen R. Mays, Dr. Timothy J. Colgan, and Dr. Matthew Burfeindt for helping me get acquainted with the subject of computational electromagnetics during the initial period of my Ph.D. I thank my colleagues Dr. Hung Luyen, James Sawicki, Luz Maria Neira, Yahya Mohtashami, Alex Haufler and Audrey Evans for their help and support.

TABLE OF CONTENTS

Page

LIST OF TABLES

LIST OF FIGURES

Figure Page

Figure Page

Figure Page

NOMENCLATURE

CEM	**C**omputational **E**lectro**m**agnetics
FDTD	**F**inite-**D**ifference **T**ime-**D**omain
FEM	**F**inite **E**lement **M**ethod
MoM	**M**ethod **o**f **M**oments
BFE	**B**asis-**F**unction **E**xpansion
HDMR	**H**igh-**D**imensional **M**odel **R**epresentation
ME-PC	**M**ulti-**E**lement **P**robabilistic **C**ollocation
PCE	**P**olynomial **C**haos **E**xpansion
HTC	**H**igh-**T**hroughput **C**omputing
HPC	**H**igh-**P**erformance **C**omputing
EFIE	**E**lectric-**F**ield **I**ntegral **E**quation
TM	**T**ransverse **M**agnetic
SAR	**S**pecific **A**bsorption **R**ate

ABSTRACT

Uncertainties in the measured electromagnetic properties of materials and uncertainties in dimensions of fabricated circuits and devices give rise to statistical uncertainties in field values obtained in computational electromagnetics (CEM) simulations. It is desirable to efficiently quantify such uncertainties resulting in the computed fields.

We have developed a classification framework for existing methods of uncertainty quantification in CEM. The existing methods have an opaque terminology that hides the mathematical strategies employed by these methods for uncertainty quantification. The framework we have developed addresses this opaque terminology by classifying the existing methods into well-defined groups with transparent terminology. This classification elucidates the relationships between the existing methods, if any. The classification framework also reveals new directions for research in the field of uncertainty quantification for CEM.

We have analyzed the accuracy and the efficiency of using polynomial models in approximating statistical field variation in CEM simulations. Canonical scatterers with dielectric uncertainties were chosen as the performance evaluation testbeds. The accuracy of polynomial approximations was shown to be strongly dependent on the mean dielectric properties of the scatterer. Extremely high-order expansions are necessary to achieve accurate approximations in some instances. The computational cost of higher-order approximations limits the utility of polynomial basis function expansions in CEM uncertainty quantification.

We have developed a new gradient estimation method using electric field integral equations to be used for sensitivity analysis in CEM. The cost of this new method does not

scale with the number of uncertain parameters. Performance evaluation using the canonical dielectric cylinder and the 2D photonic crystal waveguide branch testbeds revealed that the new method is significantly better than the difference approximation technique in accuracy and that the new method is reliable even in realistic scenarios. The cost of the new method however scales with the number of observation points.

Finally, we have investigated the impact of sampling-based uncertainty quantification methods with regards to their computational efficiency. In sampling methods, computational efficiency depends on the sampling distribution and on whether the sampling is random or deterministic. Investigation was carried out using three distinct representative examples. Uniform deterministic sampling was observed to have a significant advantage over other forms of sampling in terms of computational efficiency for all the three examples.

Chapter 1

Introduction

1.1 Background and literature review

The significant improvements made in computational capabilities in the last few decades have led to the possibility of running 3D full-wave numerical electromagnetics simulations even on personal computers. These simulations help in providing significant insight into several important applications in the vast field of applied electromagnetics. These simulations can be designed using different computational techniques or algorithms such as the finite-difference time-domain (FDTD) method [1], the finite element method (FEM) [2], and the method of moments (MoM) [3]. Such techniques collectively form the field of computational electromagnetics (CEM).

There are inherent uncertainties in the measured values describing the electric and magnetic properties of materials used in CEM simulations due to factors such as intrinsic heterogeneity and changing ambient conditions of temperature, humidity, and pressure. Similarly, the measured values describing the dimensions of the devices and circuits modeled in CEM simulations have uncertainties associated with them due to manufacturing tolerances. These uncertainties give rise to variability in the manner in which electromagnetic waves interact with the materials and devices which, in turn, gives rise to variabilities in the measured field values in CEM simulations.

The full potential of CEM simulations can be realized when computationally efficient techniques are developed to estimate the variability resulting in the electromagnetic field quantities due to known material and dimensional uncertainties incorporated into the

CEM simulations as inputs. The process of measuring such variability resulting in field quantities is called uncertainty quantification. The uncertain material and dimensional properties can be denoted as random variables and the field quantities or related quantities such as S-parameters and voltages can be modeled as functions of random variables. Uncertainty quantification in computational electromagnetics is limited to estimating the statistical parameters like mean and standard deviation of these functions of random variables in the subsequent chapters of this dissertation.

Several techniques ([4]-[14]) have been proposed in the last few years for efficient uncertainty quantification in CEM simulations. The terminology used for these proposed techniques is often opaque and not indicative of the mathematical tools and concepts employed in them for uncertainty quantification.

1.2 Motivation

The opaque terminology of the proposed uncertainty quantification methods hinders researchers from answering important questions regarding the similarities between the methods, if any, and questions regarding their relative strengths and weaknesses. Previous attempts of a literature review on such methods in CEM ([4]) have not addressed this issue of opaque terminology. There is significant advantage in drawing a big-picture understanding by studying all the mathematical concepts used by these proposed methods for uncertainty quantification. Such an understanding would help us categorize similar methods and reflect on the kind of problems that each of these methods is best suited to solve.

Many of the proposed efficient methods of uncertainty quantification in CEM ([4]-[11]) approximate the stochastically varying field quantities as polynomials in terms of random variables. The universal applicability in terms of practical computational cost is not guaranteed for such polynomial model approximation.

Sensitivity analysis is the same as uncertainty quantification in problems where the magnitudes of input uncertainties are small. For such small magnitudes of uncertainties,

approximating fields as linear functions in random variables is sufficient to perform accurate uncertainty quantification. Therefore, sensitivity analysis amounts to estimation of first-order derivatives of field variation with respect to every random variable or, in other words, estimation of the gradient of fields with respect to the multiple random variables as dimensions instead of the spatial dimensions. The techniques currently used to estimate derivatives of field variation with respect to the random variables have challenges regarding computational efficiency, accuracy, and robustness towards simulation related numerical errors.

In sampling-based uncertainty quantification methods, the computational efficiency of the uncertainty quantification procedure is observed to be dependent on the sampling distribution of the random variable. In random sampling, the efficiency is known to change for every random realization. The proposed sampling methods ([13]-[14]) have been implemented in specific applications where the results are highly accurate in order to showcase the effectiveness of these methods.

1.3 Specific research aims

Aim 1: To develop a classification framework for methods of uncertainty quantification in CEM. We have developed a classification framework for the methods of uncertainty quantification in CEM. In this framework, the methods are categorized based on the mathematical tools and concepts they use for quantifying uncertainties in field values. We have developed a transparent terminology for all the proposed methods using this framework. Furthermore, we have identified the existing similarities between the proposed methods using the framework.

Aim 2: To investigate the accuracy of polynomial approximations to the statistical field variation in canonical scattering examples involving dielectric uncertainties. We investigated the accuracy of polynomial approximations using three canonical scattering scenarios with dielectric uncertainties. Analytical expressions for field values were used

to assess the accuracy of the standard deviation of the field quantities derived from such polynomial model approximations. We identified several instances of mean dielectric properties of the canonical scatterers where such polynomial model approximation is impractical in terms of the computational cost required for uncertainty quantification.

Aim 3: To develop a sensitivity analysis technique for scattering scenarios involving a large number of sensitivity parameters and a small number of observation points. We developed a sensitivity analysis technique using electric-field integral equations where the cost of gradient estimation does not scale with the number of random variables. This makes sensitivity analysis practical even in case of a large number of random variables. The cost however scales with the number of observation points.

Aim 4: To investigate the impact of sampling techniques on the efficiency of uncertainty quantification in computational electromagnetics. We investigated random and deterministic sampling methods in terms of their impact on the computational efficiency of the uncertainty quantification procedure. We carried out the investigation in three distinct representative CEM simulation examples assuming one random variable in each. We also investigated the impacts of uniform sampling and sampling based on the distribution of the random variable on the computational efficiency of uncertainty quantification. Uniform deterministic sampling distribution provided in the most computationally efficient uncertainty quantification in each of these three distinct examples.

1.4 References

[1] A. Taflove and S. C. Hagness, *Computational Electrodynamics: The Finite-Difference Time-Domain Method*, 3rd ed. Norwood, MA: Artech House, 2005.

[2] J. M. Jin, *The Finite Element Method in Electromagnetics*, 2nd ed. New York, NY: Wiley, 2002.

[3] W. C. Gibson, *The Method of Moments in Electromagnetics*, 2nd ed. Boca Raton, FL: CRC Press, 2015.

[4] R. S. Edwards, A. C. Marvin, and S. J. Porter, "Uncertainty analyses in the finite-difference time-domain method," *IEEE Trans. Electromagn. Compat.*, vol. 52, no. 1, pp. 155–163, 2010.

[5] C. Chauviere, J. S. Hesthaven, and L. Lurati, "Computational modeling of uncertainty in time-domain electromagnetics," *SIAM J. Sci. Comput.*, vol. 28, no. 2, pp. 751–755, 2006.

[6] A. C. Yücel, H. Bagcı and E. Michielssen, "An adaptive multi-element probabilistic collocation method for statistical EMC/EMI characterization," *IEEE Trans. Electromagn. Compat.*, vol. 55, no. 6, pp. 1154–1168, 2013.

[7] Z. Zhang, T. W. Weng, and L. Daniel, "Big-data tensor recovery for high-dimensional uncertainty quantification of process variations," *IEEE Trans. Compon., Packag., Manuf. Technol.*, vol. 7, no. 5, pp. 687–697, 2017.

[8] R. Chowdhury and S. Adhikari, "High dimensional model representation for stochastic finite element analysis," *Appl. Math. Modell.*, vol. 34, no. 12, pp. 3917–3932, 2010.

[9] M. L. Gilbert and F. L. Teixeira, "A small-perturbation automatic-differentiation method for determining uncertainty in computational electromagnetics," *IEEE Trans. Antennas Propag.*, vol. 60, no. 11, pp. 5305–5314, 2012.

[10] A. C. M. Austin and C. D. Sarris, "Efficient analysis of geometrical uncertainty in the FDTD method using polynomial chaos with application to microwave circuits," *IEEE Trans. Microw. Theory Tech.*, vol. 61, no. 12, pp. 4293–4301, 2013.

[11] S. Sandeep and A. Gasiewski, "Effect of geometry on the reflectivity spectrum of radiometer calibration targets," *IEEE Geosci. Remote Sens. Lett.*, vol. 11, no. 1, pp. 84–88, 2014.

[12] S. M. Smith and C. Furse, “Stochastic FDTD for analysis of statistical variation in electromagnetic fields,” *IEEE Trans. Antennas Propag.*, vol. 60, no. 7, pp. 3343–3350, 2012.

[13] A. Galetzka, Z. Bontinck, U. Römer, and S. Schöps, “Multilevel Monte Carlo simulation of the eddy current problem with random parameters,” *2017 International Applied Computational Electromagnetics Society Symposium - Italy (ACES)*, Florence, 2017, pp. 1–2.

[14] J. P. Jacobs, S. Koziel, and S. Ogurtsov, "Computationally efficient multi-fidelity Bayesian support vector regression modeling of planar antenna input characteristics," in *IEEE Trans. Antennas Propag.*, vol. 61, no. 2, pp. 980–984, 2013.

Chapter 2

A Classification Framework for Methods in Uncertainty Quantification

2.1 Introduction

Several methods ([1]-[14]) have been proposed in the last decade for efficient uncertainty quantification in computational electromagnetics (CEM) simulations. These methods have an opaque terminology in the sense that the terminology does not clearly indicate the mathematical techniques that are employed for uncertainty quantification. However, there can be a significant advantage in drawing a big-picture understanding by studying all the mathematical concepts and tools used by the published methods for uncertainty quantification in CEM. Such an understanding would help us in organizing and classifying the methods into categories, developing an overall organizational framework or a classification framework in the process. This chapter describes in detail the classification framework we have developed for methods in uncertainty quantification.

2.2 Defining the uncertainty quantification problem in CEM

2.2.1 Modeling uncertain parameters as random variables

In CEM simulations, the uncertain dielectric and/or magnetic properties of some or all materials in the simulation domain are the most common uncertain parameters. The other common uncertain parameters are the dimensions circuits and devices. We model these uncertain parameters as random variables denoted by ξ_i where i represents the index of the random-variable. We assume that there are N such random variables. We group these N random variables together as a random vector denoted by $\boldsymbol{\xi}$.

$$\boldsymbol{\xi} = \begin{bmatrix} \xi_1 & \xi_2 & \cdots & \xi_N \end{bmatrix}^T \tag{2.1}$$

2.2.2 Modeling field quantities as functions of multiple random variables

We model field quantities or related quantities such as S-parameters and voltages as functions of multiple uncertain model parameters or random variables. The field quantities are denoted by $X(\boldsymbol{\xi})$.

$$X(\boldsymbol{\xi}) = X(\xi_1, \xi_2, \ldots, \xi_N) \tag{2.2}$$

The field quantities are either functions of space and time in time-domain CEM simulations or they are functions of space and frequency in frequency-domain CEM simulations. The fields are now modeled as functions of uncertain parameters also. These fields are therefore expressed as:

$$X(\boldsymbol{\xi}) = X(\xi_1, \xi_2, \ldots, \xi_N, t, \vec{r}) \tag{2.3}$$

or

$$X(\boldsymbol{\xi}) = X(\xi_1, \xi_2, \ldots, \xi_N, \omega, \vec{r}) \tag{2.4}$$

Here, t represents time, ω represents angular frequency and $\vec{r}$ represents position vector.

2.2.3 Considering the most general joint probability density function (PDF)

We assume the most general case with regards to the joint probability distribution of the N random variables in the vector $\boldsymbol{\xi}$. We do not make any specific assumptions about the mutual independence of or about the mutual correlation between the different random variables. We denote the generalized joint probability density function of the random vector $\boldsymbol{\xi}$ as $p(\boldsymbol{\xi})$.

$$p(\boldsymbol{\xi}) = p(\xi_1, \xi_2, \ldots, \xi_N) \tag{2.5}$$

The probability distributions in most real cases are assumed *a priori* except in a few cases where the distribution is based on actually collected statistical data.

2.2.4 Evaluating mean and variance integrals of fields

We denote the mean and variance of fields or of related quantities as $\langle X(\boldsymbol{\xi})\rangle$ and $\sigma^2\{X(\boldsymbol{\xi})\}$ respectively. Incorporating the joint probability density function, the mean and variance of $X(\boldsymbol{\xi})$ are expressed in integral forms as follows:

$$\langle X(\boldsymbol{\xi})\rangle = \int\int\cdots\int X(\boldsymbol{\xi}) p(\boldsymbol{\xi}) \mathrm{d}\xi_1 \mathrm{d}\xi_2 \cdots \mathrm{d}\xi_N \tag{2.6}$$

$$\sigma^2\{X(\boldsymbol{\xi})\} = \int\int\cdots\int (X(\boldsymbol{\xi}) - \langle X(\boldsymbol{\xi})\rangle)^2 p(\boldsymbol{\xi}) \mathrm{d}\xi_1 \mathrm{d}\xi_2 \cdots \mathrm{d}\xi_N \tag{2.7}$$

We propose a classification framework for existing uncertainty quantification methods in CEM based on:

i) the different ways of representing $X(\boldsymbol{\xi})$ in the integrands of the mean and variance integrals stated above; and

ii) the different ways of evaluating the mean and variance integrals for each of those representations.

We explain this classification framework elaborately in the subsequent sections of this chapter. The framework is composed of multiple levels of dichotomous classifications based on the steps taken at various stages of the uncertainty quantification procedure. We provide a bird's-eye view of these multiple stages of classification with the help of elaborate tree diagrams in the end. We also depict each individual dichotomous classification using a simple tree diagram indicating its location within the larger tree diagram. Furthermore, we summarize all the prominent distinguishing features for each dichotomous classification in tabular form.

2.3 Our primary classification

2.3.1 Criterion for our primary classification

We primarily classify uncertainty quantification methods in CEM into two categories namely basis-function expansion (BFE) methods and sampling methods. This classification is based on the different ways in which the field function $X(\boldsymbol{\xi})$ can be represented in terms of the uncertain model parameters.

2.3.2 BFE methods

In BFE methods, we represent the function $X(\boldsymbol{\xi})$ using a weighted sum of known basis functions in $\boldsymbol{\xi}$ denoted as $\psi_j(\boldsymbol{\xi})$ where j indicates the index of the basis-function. We assume that there are P such basis functions. We denote the weights or the unknown coefficients of these basis functions as χ_j. Using these basis functions and their corresponding coefficients, we represent the fields, $X(\boldsymbol{\xi})$, as BFEs. We summarize this representation in the following equation:

$$X(\boldsymbol{\xi}) = \sum_{j=0}^{P} \chi_j \psi_j(\boldsymbol{\xi}) \tag{2.8}$$

Based on this representation of $X(\boldsymbol{\xi})$, we write the final expressions for mean and variance of $X(\boldsymbol{\xi})$ as follows:

$$\langle X(\boldsymbol{\xi})\rangle = \sum_{j=0}^{P} \chi_j \langle \psi_j(\boldsymbol{\xi})\rangle \tag{2.9}$$

$$\sigma^2\{X(\boldsymbol{\xi})\} = \sum_{j=0}^{P} \chi_j^2 \sigma^2\{\psi_j(\boldsymbol{\xi})\} + 2\sum_{r=0}^{P}\sum_{\substack{s=0\\ s\neq r}}^{P} \chi_r\chi_s[\mathrm{Cov}\{\psi_r(\boldsymbol{\xi}), \psi_s(\boldsymbol{\xi})\}] \tag{2.10}$$

In these equations, we use $\langle\psi_j(\boldsymbol{\xi})\rangle$ and $\sigma^2\{\psi_j(\boldsymbol{\xi})\}$ to denote mean and variance of the j^{th} basis function respectively. We use $\mathrm{Cov}\{\psi_r(\boldsymbol{\xi})\,,\,\psi_s(\boldsymbol{\xi})\}$ to denote the covariance between the r^{th} and the s^{th} basis functions. The covariance is defined as the difference between the mean of the product and the product of the means. We term these three quantities namely mean, variance and covariance as statistical parameters of the basis functions. Since the basis functions are chosen *a priori*, their statistical parameters are known *a priori*. Uncertainty quantification in BFE methods amounts to calculating the coefficients in the BFEs.

2.3.3 Sampling methods

In sampling methods, we represent the function $X(\boldsymbol{\xi})$ using individual function values evaluated corresponding to sample values of the different uncertain model parameters that are part of the random vector $\boldsymbol{\xi}$. The k^{th} sample value is denoted as $\boldsymbol{\xi}^k$. Here, k represents the index of the sample values. We assume that there are M samples of the random vector $\boldsymbol{\xi}$. We denote the field function values calculated corresponding to the sample values as $X(\boldsymbol{\xi}^k)$. We use the following expressions for the mean and variance of field $X(\boldsymbol{\xi})$:

$$\langle X(\boldsymbol{\xi})\rangle = \sum_{k=1}^{M} [\lambda_k X(\boldsymbol{\xi}^k)] \tag{2.11}$$

$$\sigma^2\big\{X(\bar{\xi})\big\} \sum_{k=1}^{M} [\lambda_k X^2(\boldsymbol{\xi}^k)] - \sum_{k=1}^{M} [\lambda_k X(\boldsymbol{\xi}^k)]^2 \tag{2.12}$$

Here, λ_k represents coefficient corresponding to the function value evaluated for the k^{th} sample. The values of λ_k depend on sampling distribution and sampling density. For example, if the sampling is based on the probability distributions of the uncertain parameters and if the sampling density is very high, we can assume all λ_k to be $(1/M)$.

2.3.4 Our primary classification summarized

We depict our primary dichotomous classification of methods of uncertainty quantification in CEM in a simple tree diagram given in fig. 2.1. We summarize the distinguishing features of methods belonging to this dichotomy in table 2.1.

Table 2.1: Table describing the contrasting branches in our primary classification of uncertainty quantification methods in CEM

Distinguishing Criterion	**BFE Methods**	**Sampling Methods**
Representation of $X(\boldsymbol{\xi})$	Express $X(\boldsymbol{\xi})$ as a weighted BFE: $X(\boldsymbol{\xi}) = \sum_{j=0}^{P} \chi_j \psi_j(\boldsymbol{\xi})$	Sample $\boldsymbol{\xi}$ to obtain: $\{\boldsymbol{\xi}^k : k = 1, 2, .., M\}$; and compute $X(\boldsymbol{\xi})$ to obtain: $\{X(\boldsymbol{\xi}^k) : k = 1, 2, .., M\}$
Mean	$\langle X(\boldsymbol{\xi})\rangle = \sum_{j=0}^{P} \chi_j \langle \psi_j(\boldsymbol{\xi})\rangle$	$\langle X(\boldsymbol{\xi})\rangle = \sum_{k=0}^{M} [\lambda_k X(\boldsymbol{\xi}^k)]$ λ_k is the k^{th} sample weight
Variance	$\sigma^2\{X(\boldsymbol{\xi})\} = \sum_{j=0}^{P} \chi_j^2 \sigma^2\{\psi_j(\boldsymbol{\xi})\} + 2\sum_{r=0}^{P}\sum_{\substack{s=0 \\ s\neq r}}^{P} \chi_r \chi_s [\mathrm{Cov}\{\psi_r(\boldsymbol{\xi}), \psi_s(\boldsymbol{\xi})\}]$	$\sigma^2\{X(\boldsymbol{\xi})\} = \sum_{k=0}^{M} [\lambda_k X^2(\boldsymbol{\xi}^k)] - \sum_{k=0}^{M} [\lambda_k X(\boldsymbol{\xi}^k)]^2$

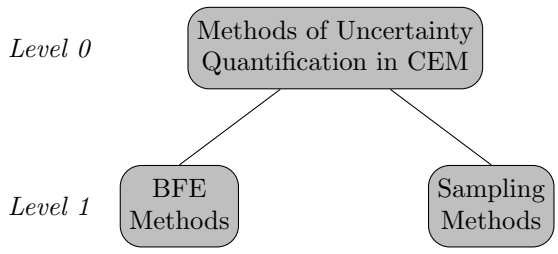

Figure 2.1: Tree diagram showing our primary classification of uncertainty quantification methods in CEM

We explain the classification of BFE methods elaborately in the next section. We similarly explain the classification of sampling methods similarly in the subsequent section.

2.4 Uncertainty quantification procedure in BFE methods

In BFE methods, we approximate the fields or the related quantities, denoted by $X(\boldsymbol{\xi})$, using a BFE. In the process, we first decide the type of basis functions to be used in the BFE. The type can be polynomial or non-polynomial like trigonometric basis functions or wavelets. We then decide the number of such basis functions P. Once the type and number of basis functions are decided, we estimate the mean and variance of $X(\boldsymbol{\xi})$ in two steps as follows:

Step 1 : Evaluation of coefficients

We evaluate the coefficients χ_j by running one modified or multiple conventional CEM simulations. We either modify the CEM algorithm so that we can evaluate all the coefficients of the BFE in one simulation directly or we run multiple conventional CEM simulations corresponding to quadrature points that are chosen *a priori* using which the coefficients of the BFE can be quickly evaluated indirectly. This step of running a one modified or multiple conventional simulations is the computationally most intensive step.

Step 2 : Evaluation of statistical parameters of basis functions

Once the coefficients are evaluated, we calculate the statistical parameters of the field functions using equations 2.9 and 2.10. The statistical parameters of the basis functions are known *a priori*. The is the computationally cheap step.

The computational accuracy of BFE methods scales with number of basis functions P and that of sampling methods scales with number of samples M. The computational cost for BFE methods can be given as that of $\mathrm{O}\big((P+1)^K\big)$ conventional CEM simulations. The value of K varies from just above 0 to 2 depending

Table 2.2: Table describing the contrasting branches in our primary classification of BFE methods

Distinguishing Criterion	**Non-polynomial BFE Methods**	**Polynomial BFE Methods**
Type of basis functions	Non-polynomial	Polynomial

on the specific BFE method used. The computational cost of sampling methods can be given as that of $\mathrm{O}(M)$ conventional CEM simulations. The BFE methods are computationally very efficient if the appropriate basis functions for the given problem are used. However, appropriate basis functions for a given problem of uncertainty quantification are not known *a priori*. Indirect coefficient estimation is easy to implement and is suitable for High-Throughput Computing (HTC) platforms. The direct coefficient estimation requires change in algorithm and is suitable for a High-Performance Computing (HPC) platform.

We now classify BFE methods starting with the type of basis functions used in the BFE.

2.4.1 Our primary classification of BFE methods

Our primary classification of BFE methods is based on whether the basis functions used are polynomial or non-polynomial in nature. Our primary classification of BFE methods is shown in a tree-diagram in fig. 2.2. Table 2.2 distinguishes between the two branches in the classification. The two branches in this classification are elaborately explained in the next two sections.

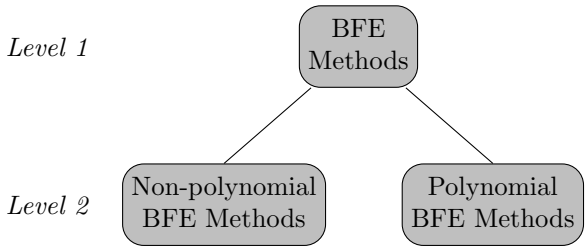

Figure 2.2: Tree diagram showing our primary classification of BFE methods

2.4.2 Non-polynomial BFE methods

In these methods, the basis functions $\psi_j(\boldsymbol{\xi})$ are non-polynomial in nature like trigonometric basis functions or wavelets for example. To the best of our knowledge, there has been only a limited attempt of using non-polynomial basis functions in a BFE-based uncertainty quantification method so far like the one using wavelets [1]. Hence, we have not classified non-polynomial BFE methods any further.

2.4.3 Polynomial BFE methods

In these methods, the basis functions $\psi_j(\boldsymbol{\xi})$ are polynomial in nature. The polynomial BFE methods are the most widely published methods in the field of uncertainty quantification. The polynomial BFE methods are further classified based on whether the BFE is an orthogonal polynomial BFE or a Taylor-series expansion. This classification is shown in a tree-diagram in fig. 2.3. Table 2.3 distinguishes between the two branches in the classification. It can be proven that any polynomial function of $\boldsymbol{\xi}$ can be modeled both by using orthogonal polynomial basis functions and by using terms in the Taylor-series expansion.

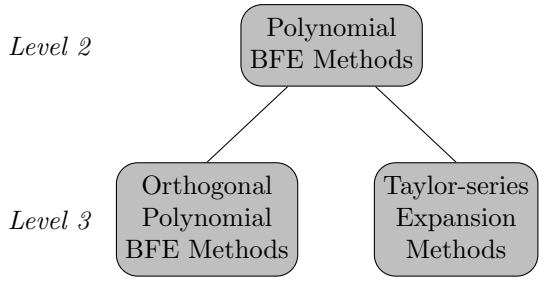

Figure 2.3: Tree diagram showing our classification of polynomial BFE methods

In table 2.3, $\phi^{\{i,j\}}(\xi_i)$ represents an orthogonal polynomial in ξ_i where index i represents i^{th} random variable and index j represents j^{th} basis function. So, $\phi^{\{i,j\}}(\xi_i)$ represents the orthogonal polynomial in the i^{th} random variable ξ_i which is part of a continuous product of orthogonal polynomials in all N random variables to form the complete j^{th} basis function $\psi_j(\boldsymbol{\xi})$:

$$\psi_j(\boldsymbol{\xi}) = \prod_{i=1}^{N} \phi^{\{i,j\}}(\xi_i)$$

ξ_i^0 represents the value in the i^{th} random variable at which the partial derivative with respect to the random variable is calculated. Operator $||\cdot||_{2,w}$ represents $\mathcal{L}^2$ norm with $w(\cdot)$ as the weighting function. Usually the weighting function is the joint probability distribution of the random variables, $p(\cdot)$, but it need not necessarily be so.

In table 2.3, the Taylor-series expansion for the stochastic function $X(\boldsymbol{\xi})$ is valid in the neighborhood of the point $\boldsymbol{\xi}^0$ at which the derivative is computed. In the methods based on Taylor-series expansion, the coefficients are partial derivatives of $X(\boldsymbol{\xi})$ of varying orders and dimensions. These partial derivatives are calculated at $\boldsymbol{\xi} = \boldsymbol{\xi}^0$ and can be expressed as $\left.\frac{\partial^{n_1}\partial^{n_2}\cdots\partial^{n_N}X(\boldsymbol{\xi})}{\partial\xi_1^{n_1}\partial\xi_2^{n_2}\cdots\partial\xi_N^{n_N}}\right|_{\boldsymbol{\xi}=\boldsymbol{\xi}^0}$. Here, it is assumed that the Taylor-series expansion is of order D. Also, the coefficient and the polynomial are each given a subscript j but

Table 2.3: Table describing the contrasting branches in our classification of Polynomial BFE methods

Distinguishing Criterion	**Orthogonal Polynomial BFE Methods**	**Taylor-series Expansion Methods**
Polynomial basis functions	$\psi_j(\boldsymbol{\xi}) = \prod_{i=1}^{N} \phi^{\{i,j\}}(\xi_i)$ where $\phi^{\{i,j\}}$: Orthogonal polynomial in ξ_i	$\psi_j(\boldsymbol{\xi}) = \prod_{i=1}^{N} \frac{\left(\xi_i - \xi_i^0\right)^{n_i}}{n_i!}$
Field quantities	$X(\boldsymbol{\xi}) = \sum_{j=0}^{P} \chi_j \left(\prod_{i=1}^{N} \phi^{\{i,j\}}(\xi_i) \right)$	$X(\boldsymbol{\xi}) = \sum_{\substack{n_1=0 \\ \sum_i n_i \leq D}}^{D} \cdots \sum_{n_N=0}^{D} \left[\frac{\partial^{n_1}\partial^{n_2}\cdots\partial^{n_N} X(\boldsymbol{\xi})}{\partial\xi_1^{n_1}\partial\xi_2^{n_2}\cdots\partial\xi_N^{n_N}}\Big\vert_{\boldsymbol{\xi}=\boldsymbol{\xi}^0} \cdot \prod_{i=1}^{N} \frac{\left(\xi_i - \xi_i^0\right)^{n_i}}{n_i!} \right]$
Coefficients	$\chi_j = \left(\frac{1}{\|\|\psi_j(\boldsymbol{\xi})\|\|_{2,w}^2} \right) \int \psi_j(\boldsymbol{\xi}) X(\boldsymbol{\xi}) w(\boldsymbol{\xi}) \mathrm{d}\boldsymbol{\xi}$	$\chi_j = \frac{\partial^{n_1}\partial^{n_2}\cdots\partial^{n_N} X(\boldsymbol{\xi})}{\partial\xi_1^{n_1}\partial\xi_2^{n_2}\cdots\partial\xi_N^{n_N}}\Big\vert_{\boldsymbol{\xi}=\boldsymbol{\xi}^0}$
Tools for evaluation of coefficients	Orthogonality conditions	Derivative estimation techniques like difference approximation

expressed only in terms of orders in individual random variables i.e., n_i. This will be explained in detail in the subsection on Taylor-series expansion methods.

2.4.3.1 Orthogonal polynomial BFE methods

In these BFE methods, the basis functions are continuous products of orthogonal polynomials in individual random variables. All the orthogonal polynomials of a particular random variable must be of the same class and this class can be Hermite, Jacobi, Laguerre, Legendre or even a class that is custom-defined specifically for the problem. These classes of polynomials vary based on the different weighting functions associated with their $\mathcal{L}^2$ norms. However, orthogonal polynomials of two different random variables need not be of the same class. In other words, the polynomials in the i^{th} random variable can be of Hermite class and the polynomial in the $(i+1)^{\text{th}}$ random variable can be of Legendre class and so on. It can be proven that any polynomial function of $\boldsymbol{\xi}$ can be modeled as an orthogonal polynomial BFE of this kind with the appropriate coefficients. As basis functions are continuous products of the chosen orthogonal polynomials in individual random variables, any two basis functions are also considered to be orthogonal. The weighting function associated with the $\mathcal{L}^2$ norm of a basis function is the continuous product of the weighting functions of orthogonal polynomials in individual random variables that make up the basis function. Usually the weighting function is the joint probability distribution of the random variables, $p(\cdot)$, but it need not necessarily be so.

$$\int \phi^{\{i,r\}}(\xi_i)\phi^{\{i,s\}}(\xi_i)w_i(\xi_i)\mathrm{d}\xi_i = \delta_{rs}\left|\left|\phi^{\{i,r\}}(\xi_i)\right|\right|^2_{2,w_i} \tag{2.13}$$

$$\psi_r(\boldsymbol{\xi}) = \prod_{i=1}^{N}\phi^{\{i,r\}}(\xi_i) \tag{2.14}$$

$$w(\boldsymbol{\xi}) = \prod_{i=1}^{N} w_i(\xi_i) \tag{2.15}$$

$$\implies \int \psi_r(\boldsymbol{\xi})\psi_s(\boldsymbol{\xi})w(\boldsymbol{\xi})\mathrm{d}\boldsymbol{\xi} = \delta_{rs}\left|\left|\psi_r(\boldsymbol{\xi})\right|\right|^2_{2,w} \tag{2.16}$$

Here, $w_i(\xi_i)$ represents weighting function associated with $\mathcal{L}^2$ norm of $\phi^{\{i,r\}}(\xi_i)$ and $w(\boldsymbol{\xi})$ represents weighting function associated with $\mathcal{L}^2$ norm of $\psi_r(\boldsymbol{\xi})$. δ_{rs} represents Kronecker delta for indices r and s. Operator $\left|\left|\cdot\right|\right|_{2,w}$ represents $\mathcal{L}^2$ norm with weighting function $w(\cdot)$.

Our classification of the orthogonal polynomial BFE methods is based on whether the coefficients of the BFE are directly estimated or indirectly estimated and the classification is shown in a tree-diagram in fig. 2.4. Table 2.4 distinguishes between the two branches in the classification.

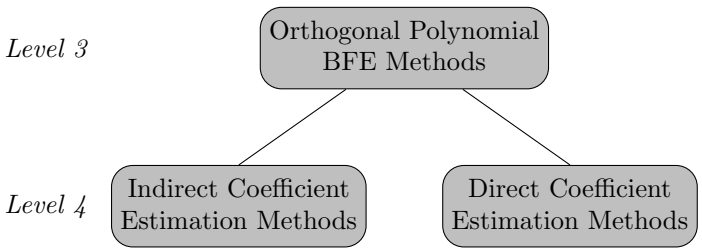

Figure 2.4: Tree diagram showing our classification of orthogonal polynomial BFE methods

In table 2.4, $\boldsymbol{\xi}^q$ represents the q^{th} quadrature point of $\boldsymbol{\xi}$. Q represents total number of quadrature points.

Estimating coefficients indirectly using quadratures

In these methods, the coefficients are given integral expressions devised using the orthogonal properties of the basis functions chosen. The stochastic function $X(\boldsymbol{\xi})$ forms a part of the integrand in these integral expressions. The integrand in these integrals is therefore in the form of polynomial times a weighting function in $\boldsymbol{\xi}$ which is ideal to be solved using quadrature points. The evaluations of the $X\,()$ values corresponding to all the quadrature points is the computationally most intensive part of the whole uncertainty quantification procedure in these methods.

The domain of integration of these integrals can be divided into smaller sub-domains and the integrals can be solved separately in each of these sub-domains using quadratures to improve the overall accuracy of coefficient estimation. There are methods published where there is no division into sub-domains like the general probabilistic collocation method [2]. The division into sub-domains can be done adaptively where accuracy of the quadrature estimate of the integral is compared before and after every step of division into sub-domains as seen in the multi-element probabilistic collocation (ME-PC) method [4]. The division into sub-domains can also be non-adaptive or fixed in nature based on approximation theories like the high-dimensional model representation (HDMR) theory. In [3], both fixed sub-domain division using HDMR and adaptive sub-domain division using ME-PC is implemented simultaneously.

The number of coefficients $P+1$ when the number of random variables is N and the order of the BFE polynomial is D is given by [2]:

$$P+1 = \frac{(N+D)!}{N!D!} \tag{2.17}$$

The accuracy of these methods scales with P. The computational cost can be estimated to be as that of $\mathrm{O}\big((P+1)^K\big)$ conventional CEM simulations where K varies from significantly less than 1 to nearly 2 for the various methods used i.e. [2], [3] and [4]. The main advantage of these methods is that the algorithm used is

Table 2.4: Table describing the contrasting branches in our classification of orthogonal polynomial BFE methods

Distinguishing Criterion	**Indirect Coefficient Estimation Methods**	**Direct Coefficient Estimation Methods**
Procedure of coefficient estimation	Indirect estimation using integrals: $\chi_j = \left(\frac{1}{\|\|\psi_j(\boldsymbol{\xi})\|\|^2_{2,w}}\right)\int \psi_j(\boldsymbol{\xi})X(\boldsymbol{\xi})w(\boldsymbol{\xi})\mathrm{d}\boldsymbol{\xi}$ which are solved using quadratures: $\chi_j = \left(\frac{1}{\|\|\psi_j(\boldsymbol{\xi})\|\|^2_{2,w}}\right)\sum_{q=1}^{Q} \psi_j(\boldsymbol{\xi}^q)X(\boldsymbol{\xi}^q)w(\boldsymbol{\xi}^q)$	In the CEM algorithm, i) substitute BFEs for fields, ii) use orthogonal property of basis functions in each step, to obtain expressions for a direct coefficient estimation
Computationally most intensive step	The multiple deterministic CEM simulations to evaluate $X(\boldsymbol{\xi}^q)$	The modified CEM simulation to estimate χ_j, $j = 1$ to P

the already established conventional deterministic CEM algorithm without modifications. The simulations corresponding to the various quadrature points can be run in parallel on a HTC platform.

Hence, the orthogonal polynomial BFE methods with indirect coefficient estimation can be divided into three final categories as shown in the tree diagram in fig. 2.5. Table 2.5 distinguishes between the branches listed in the classification shown in fig. 2.5.

Estimating coefficients directly by modifying the CEM algorithm

In these methods, each step in the standard CEM algorithm meant to evaluate fields, $X(\boldsymbol{\xi})$, is modified in multiple steps so that it evaluates the coefficients in the BFE, χ_j, $j = 1$ to P, directly. This modification is done by exploiting the orthogonality of basis functions in the BFE using the Galerkin methods. This modified simulation which directly computes the coefficients in the BFE is the computationally most intensive part of the whole uncertainty quantification procedure.

The number of coefficients $P + 1$ when the number of random variables is N and the order of the BFE polynomial is D is given by equation 2.17.

For large N and D, P is very large. Many of these coefficients may be small in magnitude which do not contribute significantly to the BFE. The evaluation of coefficients of such small magnitudes can be avoided in the modified CEM algorithm. In other words, such coefficients and their associated basis functions can be omitted from the BFE. There are methods published with no such omission of coefficients like the generalized polynomial chaos expansion (PCE) ([2,[9]). Also, the omission of coefficients can be done adaptively as in [6]. The omission of coefficients can also be non-adaptively or in a fixed manner based on any approximation theories like the HDMR as in [5].

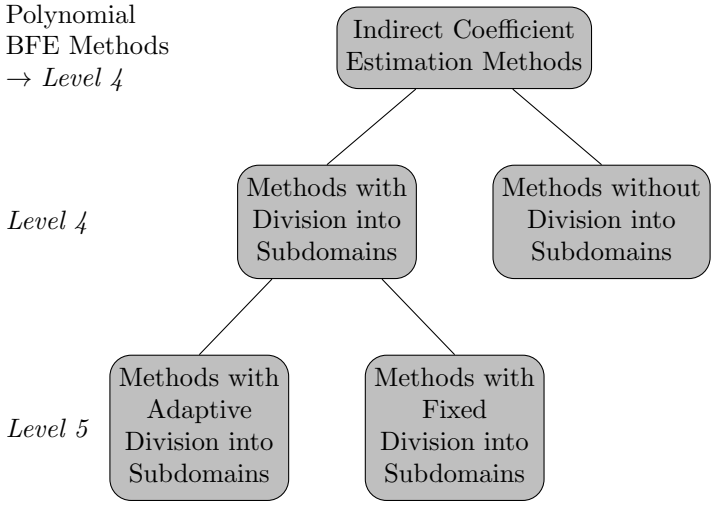

Figure 2.5: Tree diagram showing our classification of orthogonal polynomial BFE methods with indirect coefficient estimation

The accuracy of these methods scales with P. The computational cost can be estimated to be as that of $\mathrm{O}\big((P+1)^K\big)$ conventional CEM simulations where K varies from nearly 2 for non-adaptive methods to anywhere from significantly less than 1 to nearly 2 for the adaptive methods. The main disadvantage of these methods is the need to develop a modified complex algorithm based on which a single simulation can be run to obtain all the coefficients. This single simulation cannot be broken down into completely independent parts and run in parallel on a HTC platform. However, the algorithm can be parallelized locally on a HPC machine the procedure of which can get further more complicated.

Hence, the orthogonal polynomial BFE methods with direct coefficient estimation can be divided into three final categories as shown in the tree diagram in fig. 2.6. Table 2.6 distinguishes between the branches listed in the classification shown in fig. 2.6.

2.4.3.2 Taylor-series expansion methods

In these BFE methods, the stochastic field function is expressed in the multi-variable Taylor-series expansion in terms of the random variables centered at a point $\boldsymbol{\xi}^0$ in the sample space as follows:

$$X(\boldsymbol{\xi}) = \sum_{\substack{n_1=0 \\ \sum_i n_i \le D}}^{D} \cdots \sum_{n_N=0}^{D} \left[\frac{\partial^{n_1}\partial^{n_2}\cdots\partial^{n_N} X(\boldsymbol{\xi})}{\partial\xi_1^{n_1}\partial\xi_2^{n_2}\cdots\partial\xi_N^{n_N}}\bigg|_{\boldsymbol{\xi}=\boldsymbol{\xi}^0} \cdot \prod_{i=1}^{N} \frac{(\xi_i - \xi_i^0)^{n_i}}{n_i!} \right] \tag{2.18}$$

Here, each coefficient is a partial derivative estimated at the point $\boldsymbol{\xi}^0$. The coefficients are partial derivatives of different orders from 0 to D and of different dimensions from 0 to N. The number n_i represents the

Table 2.5: Table describing the contrasting branches in our classification of orthogonal polynomial BFE methods with indirect coefficient estimation

Distinguishing Criterion	**Methods with Division into Subdomains**	**Methods without Division into Subdomains**
Procedure of integral evaluation	Division of integral domain into subdomains and separate integral evaluation in each subdomain	No division of integral domain into subdomains and only one integral evaluation
Procedure of division of integral domain	Can be adaptive or fixed	No division

Table 2.6: Table describing the contrasting branches in our classification of orthogonal polynomial BFE methods with direct coefficient estimation

Distinguishing Criterion	**Methods with Omission of Coefficients**	**Methods without Omission of Coefficients**
Procedure used in modified CEM routine	Only significantly contributing coefficients computed in modified CEM routine	All coefficients computed in modified CEM routine
Procedure of omission of coefficients	Can be adaptive or fixed	No omission

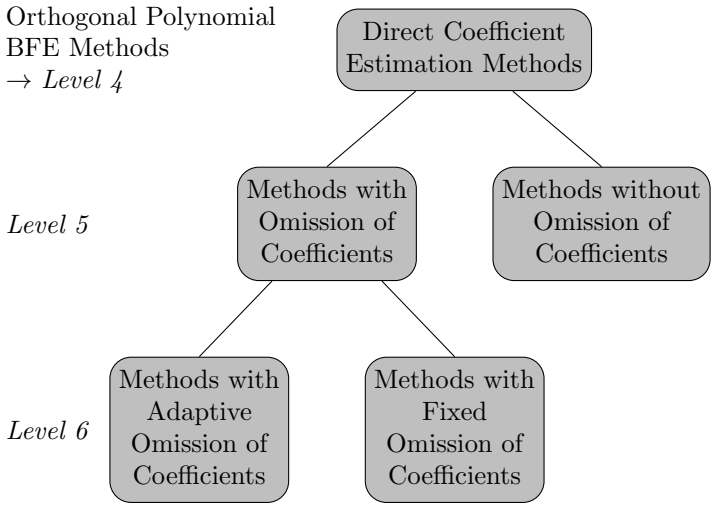

Figure 2.6: Tree diagram showing our classification of orthogonal polynomial BFE methods with direct coefficient estimation

order of derivative of field function with respect to the i^{th} random variable ξ_i. The order of the total polynomial expansion is D and hence we have the limitation that $\sum_i n_i \leq D$. The number of such coefficients or partial derivatives $P+1$ for order D and with N random variables can be given by equation 2.17.

In table 2.3, we have written the coefficient and polynomial part of this expression with a subscript j. We meant that j varies from 0 to P as there are $P+1$ coefficients and polynomials. Nevertheless, the single-term index j can be translated to an N-term index $\{n_1 n_1 n_2 \cdots n_N\}$ with a condition on the individual parts of the N-term index that $\sum_i n_i \leq D$.

The coefficients are derivatives of the field function $X(\cdot)$ that can be estimated either directly or indirectly and our primary classification of Taylor-series expansion methods is based on this distinction. The classification is shown in figure 2.7. Table 2.7 distinguishes between the branches listed in the classification shown in fig. 2.7.

Direct Estimation of Derivatives

In these methods, the coefficients of Taylor-series expansion or derivatives of field functions with respect to random variables are directly computed by incorporating the derivative calculation in the the CEM algorithm. The most common direct derivative estimation method used is the auto-differentiation. The Taylor-series expansion may be truncated to orders less than 2 which are meant to be used in sensitivity analysis problems like in [7]. The expansion can retain higher order derivative terms without truncation as in [8]. The classification of Taylor-series expansion methods with direct derivative estimation into methods

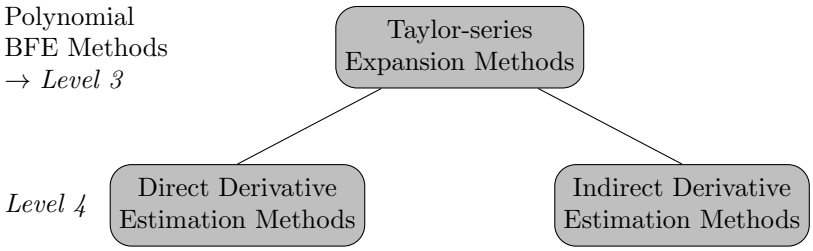

Figure 2.7: Tree diagram showing our classification of of Taylor-series expansion methods

using low-order Taylor-series expansion and methods using high-order Taylor series expansion is shown in figure 2.8.

The accuracy of these methods scales with D for a fixed N. The computational cost can be estimated as that of $\mathrm{O}(N)$ conventional CEM simulations for sensitivity analysis problems where the expansion is truncated to be of first or second order. The computational cost of a higher-order Taylor series expansion can be estimated as that of $\mathrm{O}\big((P+1)^K\big)$ conventional CEM simulations where K varies from almost 1 to nearly 2. The main disadvantage of these methods is the possibility of numerical errors from CEM simulations heavily undermining the accuracy of derivative estimation especially for higher order derivatives. Also, the CEM algorithm has to be altered for these methods.

Indirect Estimation of Derivatives

In these methods, the coefficients of Taylor-series expansion or derivatives of field functions with respect to random variables are indirectly computed by using techniques like difference approximation or adjoint sensitivity. For example, the difference approximation of the first-order derivative of the field function $X(.)$ with respect to i^{th} random variable ξ_i can be written as:

$$\frac{\partial X(\ldots,\xi_i,\ldots)}{\partial \xi_i} \approx \frac{X(\ldots,\xi_i+\Delta,\ldots)-X(\ldots,\xi_i,\ldots)}{\Delta} \tag{2.19}$$

The idea of difference approximation can be extended to estimate higher order derivatives. Difference approximation requires a convergence test to identify the ideal magnitude of difference for high accuracy which increases the computational cost of the method. Also, the numerical errors in deterministic CEM simulations can be so high that the difference approximation technique would never provide an accurate result for derivative estimation no matter how ideal the chosen magnitude of difference is. Even adjoint sensitivity analysis which is based on modifying the Maxwell's differential equations to obtain the derivatives suffers when there are large numerical errors in CEM simulations. An alternate integral equation-based indirect

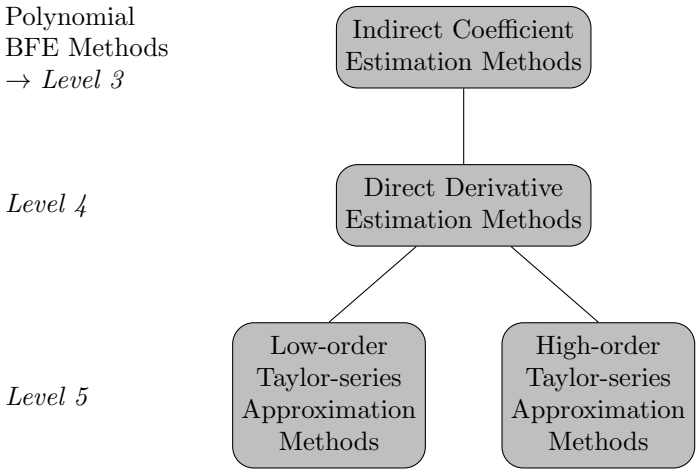

Figure 2.8: Tree diagram showing our classification of Taylor-series expansion methods with direct derivative estimation

derivative estimation technique that we developed is mentioned in chapter 4. The classification of Taylor-series expansion methods with indirect derivative estimation into methods using low-order Taylor-series expansions and methods using high-order Taylor series expansions is shown in figure 2.9. A difference approximation based low-order Taylor series expansion method is proposed in [9] where it is termed as method of moments. Adjoint sensitivity analysis that is suitable for high order Taylor series expansion even with nonlinear media is proposed in [10].

2.4.4 Classification of BFE methods summarized

We summarize the classification of BFE methods in the tree diagram given in fig. 2.10.

2.5 Uncertainty quantification procedure in sampling methods

2.5.1 Our primary classification of sampling methods

In sampling methods, the primary step is to sample the random variables at different points in the sample space and to run conventional deterministic CEM simulations corresponding to those sample points to obtain field values at those sample points. Sampling methods vary from each other in terms of the sampling strategy used. The sampling can be done once and the corresponding field values can be obtained for estimating mean and variance. Instead, the sampling can be repeated several times or in multiple levels. In multi-level sampling, field values corresponding to sample values are evaluated after every level of sampling. The useful field information obtained at the end of every level is used to perform a better

Table 2.7: Table describing the contrasting branches in our classification of orthogonal polynomial BFE methods

Distinguishing Criterion	**Indirect Derivative Estimation Methods**	**Direct Derivative Estimation Methods**
Procedure of derivative estimation	Indirect estimation using techniques like difference approximation: $\frac{\partial X(\ldots,\xi_i,\ldots)}{\partial \xi_i} \approx \frac{X(\ldots,\xi_i+\Delta,\ldots)-X(\ldots,\xi_i,\ldots)}{\Delta}$	In the CEM algorithm, i) apply derivatives to fields in update expressions, ii) obtain update expressions for derivatives of fields, for a direct derivative estimation
Computationally most intensive step	The multiple deterministic CEM simulations to evaluate derivatives	The modified CEM simulation to estimate the derivatives

sampling in the next level. The mean and variance are estimated after every level of sampling. The rate of convergence of these mean and variance estimates is tracked carefully after every level of sampling. The sampling and field evaluations are stopped once the desired convergence in the mean and variance estimates is reached. The classification of sampling methods into one-time sampling methods and multi-level sampling methods is shown in figure 2.11. Table 2.8 distinguishes between the branches listed in the classification shown in fig. 2.11.

The contents of table 2.8 will be explained in the next two subsections.

2.5.2 One-time sampling methods

In these methods, sampling of the random variables $\boldsymbol{\xi}$ is done just once to obtain the appropriate sample points $\{\boldsymbol{\xi}^k : k = 1, 2, \ldots, M\}$ corresponding to which the field values $\{X(\boldsymbol{\xi}^k) : k = 1, 2, \ldots, M\}$ are calculated using which the mean and variance of field values can be estimated. The expressions for mean and variance of field values in case of M samples are given as:

$$\langle X(\boldsymbol{\xi})\rangle = \sum_{k=1}^{M} [\lambda_k X(\boldsymbol{\xi}^k)] \tag{2.20}$$

$$\sigma^2\{X(\boldsymbol{\xi})\} = \sum_{k=1}^{M} [\lambda_k X^2(\boldsymbol{\xi}^k)] - \sum_{k=1}^{M} [\lambda_k X(\boldsymbol{\xi}^k)]^2 \tag{2.21}$$

Here, λ_k refers to the sample weights which depend on the sampling strategy in relation to the assumed probability distribution of the uncertain model parameters. For example, if the random variables are all having normal distributions and the sampling is also based on normal distribution, then the values of all λ_k would be uniformly $1/M$. The one-time sampling methods may be based on sparse sampling strategies like

Table 2.8: Table describing the contrasting branches in our primary classification of sampling methods

Distinguishing Criterion	**Multi-level Sampling Methods**	**One-time Sampling Methods**
Representation of	Sample $\boldsymbol{\xi}$ to obtain: $\{\boldsymbol{\xi}^{k_l} : k_l = 1, 2, \ldots, M_l\}$; and compute $X(\boldsymbol{\xi})$ to obtain: $\{X(\boldsymbol{\xi}^{k_l}) : k_l = 1, 2, \ldots, M_l\}$ for every level $l = 1, 2, 3, \ldots, L$	Sample $\boldsymbol{\xi}$ to obtain: $\{\boldsymbol{\xi}^{k} : k = 1, 2, \ldots, M\}$; and compute $X(\boldsymbol{\xi})$ to obtain: $\{X(\boldsymbol{\xi}^{k}) : k = 1, 2, \ldots, M\}$
Mean	$\langle X(\boldsymbol{\xi})\rangle_l = \sum_{k_l=0}^{M_l} [\lambda_{k_l} X(\boldsymbol{\xi}^{k_l})]$ λ_{k_l} is the k_l^{th} sample weight	$\langle X(\boldsymbol{\xi})\rangle = \sum_{k=0}^{M} [\lambda_{k} X(\boldsymbol{\xi}^{k})]$ λ_{k} is the k^{th} sample weight
Variance	$\sigma_l^2\{X(\boldsymbol{\xi})\} =$ $\sum_{k_l=1}^{M_l} [\lambda_{k_l} X^2(\boldsymbol{\xi}^{k_l})] - \sum_{k_l=1}^{M_l} [\lambda_{k_l} X(\boldsymbol{\xi}^{k_l})]^2$	$\sigma^2\{X(\boldsymbol{\xi})\} =$ $\sum_{k=0}^{M} [\lambda_{k} X^2(\boldsymbol{\xi}^{k})] - \sum_{k=0}^{M} [\lambda_{k} X(\boldsymbol{\xi}^{k})]^2$

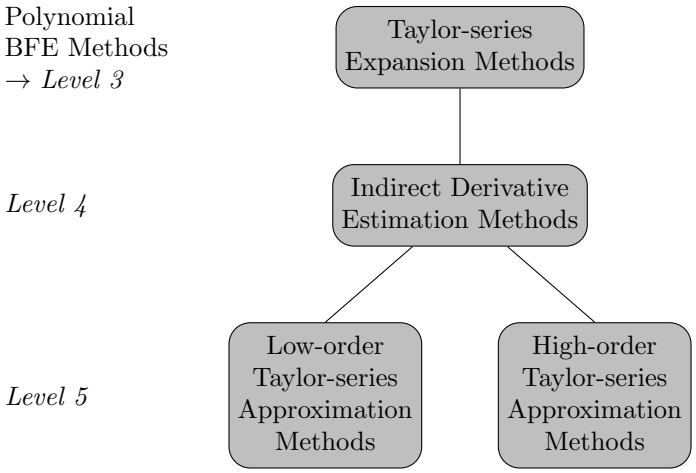

Figure 2.9: Tree diagram showing our classification of Taylor-series expansion methods with indirect derivative estimation

the Kalman-filter based unscented transformation [11]. The one-time sampling method can also be based on dense sampling strategies like the standard Monte Carlo method [9]. The classification of one-time sampling methods into sparse sampling methods and dense sampling methods is shown in figure 2.12.

The main disadvantage of this method is that the sampling does not provide any room for improvement. Most realistic scenarios are such that we have no information of field variation with respect to uncertain parameters *a priori*. Hence, it is not possible to have samples chosen suitably for computational efficiency in case of one-time sampling. However, the simulations corresponding to each sample value can be run in parallel, if possible, on a HTC platform. The computational accuracy and cost of these methods scale with the number of samples M.

2.5.3 Multi-level sampling methods

In these methods, sampling of the random variables $\boldsymbol{\xi}$ is done more than one time or in more than one level. Let the sampling be done in levels $l = 1, 2, 3, \ldots, L$. Sampling of the random variables $\boldsymbol{\xi}$ is done at each level l to obtain the appropriate sample points $\{\boldsymbol{\xi}^{k_l} : k_l = 1, 2, \ldots, M_l\}$ corresponding to which the field values $\{X(\boldsymbol{\xi}^{k_l}) : k_l = 1, 2, \ldots, M_l\}$ are calculated using which the mean and variance of field values can be estimated at the level l. The mean and variance estimates are then obtained for each level using expressions similar to 2.20 and 2.21 respectively. The field variation information along with the convergence information of mean and standard deviation estimates obtained in one level of sampling can inform the way sampling is done in another level in order to improve the computational efficiency of the uncertainty quantification procedure. This can be done in many ways. The multiple levels can be used to cover the

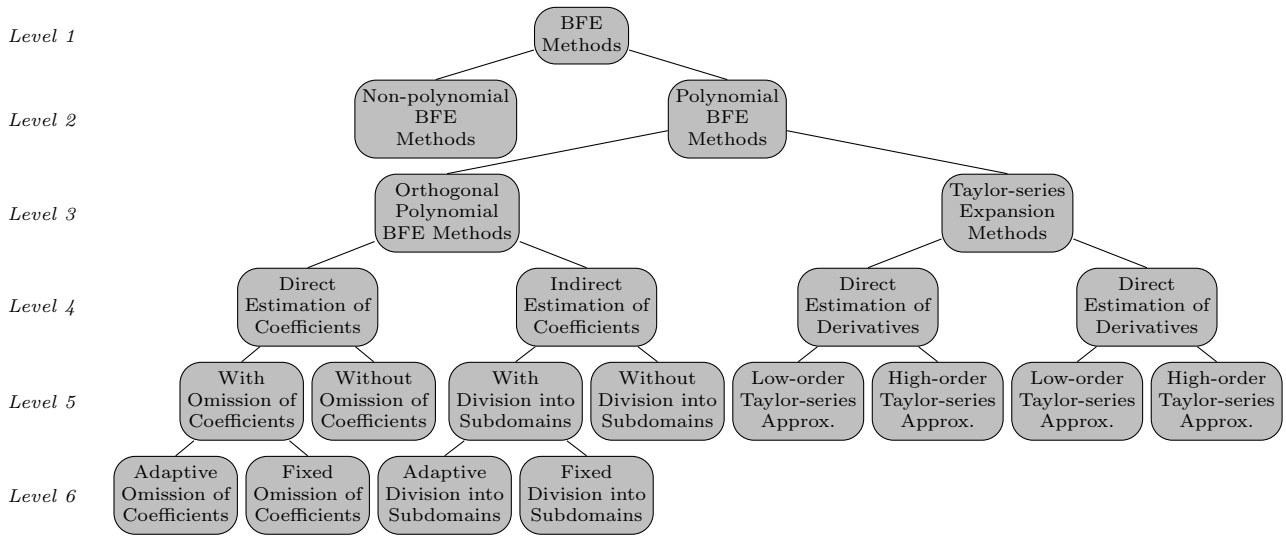

Figure 2.10: Tree diagram summarizing our classification of BFE methods

high number of dimensions efficiently in problems with a large number of uncertain parameters [12]. The multiple levels can be used to improve the sampling using Bayesian learning strategies like in the Markov Chain Monte Carlo methods [13]. The multiple levels can be the two different levels used in a mixed fidelity method also [14]. In a mixed fidelity method, the sampling is done in two levels where one level of sampling is very dense and the other is sparse. For the dense set of samples, either a no-cost surrogate model or low-cost, low-accuracy CEM simulations are used to obtain the field values corresponding to samples. Such a solution is called a low fidelity solution. For the sparse set of samples, high-cost and high-accuracy CEM simulations are used to obtain the field values corresponding to samples and such a solution is called a high fidelity solution. In a mixed fidelity method, the low fidelity solution and the high fidelity solution is combined in a unique way to get an accurate mixed fidelity solution.

In many realistic scenarios, we have very smooth variation of field quantities with respect to random variables. Such a smooth variation can be easily captured using field values evaluated corresponding to a small number of samples in a one-time sampling strategy. In these cases, multi-level sampling proves to be overkill. Sometimes, the field information obtained from simulations might have misleading level of numerical errors in them. In these cases, multi-level sampling will prove to be counter productive. Similarly, in case of mixed-fidelity methods, the low fidelity information obtained might be completely unreliable to be used in a mixed fidelity solution.

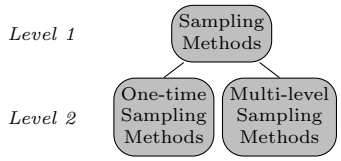

Figure 2.11: Tree diagram showing our primary classification of sampling methods

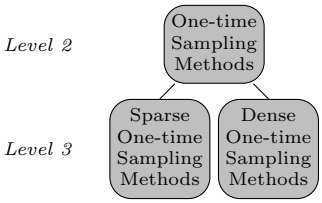

Figure 2.12: Tree diagram showing our classification of one-time sampling methods

The biggest advantage of multi-level sampling technique is the effective use of computational resources by sampling efficiently at appropriate places in the sample space. This is very helpful when the computational resources available are limited. The computational accuracy and cost of these methods scale with the total number of samples $\sum_{l=1}^{L} M_l$.

2.5.4 Classification of sampling methods summarized

We summarize the classification of sampling methods in the tree diagram given in fig. 2.13.

2.6 Conclusions

The classification framework presented here enables a systematic categorization of known methods in uncertainty quantification in CEM. The framework offers a standardized terminology and elucidates relationships between existing methods. The framework can be used to categorize all the published methods in the field of uncertainty quantification in CEM into specific groups that are defined within the framework with a transparent terminology. We can observe the distribution of the methods into the different groups in the framework and get an idea of which mathematical techniques are well developed and properly implemented and which ones are in the early stages of development and/or application. For example, we can say that a lot of work has been done regarding polynomial BFE methods but very limited work has been done regarding non-polynomial BFE methods. Thus, the framework reveals directions for future research in this field. New techniques that mix mathematical techniques from different groups mentioned in the framework can also be developed, if possible.

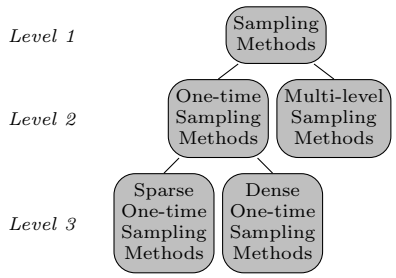

Figure 2.13: Tree diagram summarizing our classification of sampling methods

2.7 References

[1] L. Wand and C. D. Sarris, "A multi-resolution FDTD method for uncertainty quantification in the time-domain modeling of microwave structures," in IEEE MTT-S International Microwave Symposium, Tampa, Fl, USA, 2014

[2] C. Chauviere, J. S. Hesthaven, and L. Lurati, "Computational modeling of uncertainty in time-domain electromagnetics," *SIAM J. Sci. Comput.*, **28**, 2, pp. 751–755, 2006.

[3] A. C. Yücel, H. Bagcı, and E. Michielssen, "An ME-PC enhanced HDMR method for efficient statistical analysis of multiconductor transmission line networks," *IEEE Trans. Compon., Packag., Manuf. Technol.*, **5**, 5, pp. 685–696, 2015.

[4] A. C. Yücel, H. Bagcı, and E. Michielssen, "An adaptive multi-element probabilistic collocation method for statistical EMC/EMI characterization," *IEEE Trans. Electromagn. Compat.*, **55**, 6, pp. 1154–1168, 2013.

[5] S. Ganta, B. D. Van Veen, and S. C. Hagness, "On the computational complexity of polynomial chaos expansion for FDTD-based uncertainty analyses," in *2015 North American Radio Science Meeting*, Vancouver, BC, Canada, 2015.

[6] G. Blatman and B. Sudret, "Adaptive sparse polynomial chaos expansion based on least angle regression,"
textitJ. Comput. Phys., **230**, 6, pp. 2345–2367, 2011.

[7] M. S. Gilbert and F. L. Teixeira, "A small-perturbation automatic-differentiation method for determining uncertainty in computational electromagnetics," *IEEE Trans. Antennas Propag.*, **60**, 11, pp. 5305–5314, 2012.

[8] J. I. Toivanen and R. A. E. Mäkinen, "Implementation of sparse forward mode automatic differentiation with application to electromagnetic shape optimization," *Optim. Methods Softw.*, **26**, 4-5, pp. 601–606, 2011.

[9] R. S. Edwards, A. C. Marvin, and S. J. Porter, "Uncertainty analyses in the finite-difference time-domain method," *IEEE Trans. Electromagn. Compat.*, **52**, 1, pp. 155–163, 2010.

[10] M. H. Bakr, O. S. Ahmed, M. H. El Sherif, and T. Nomura, "Time domain adjoint sensitivity analysis of electromagnetic problems with nonlinear media,", *Opt. Express*, **22**, 9, pp. 10831–10843, 2014

[11] S. Sandeep and A. Gasiewski, "Effect of geometry on the reflectivity spectrum of radiometer calibration targets," *IEEE Geosci. Remote Sens. Lett.*, **11**, 1, pp. 84–88, 2014.

[12] K. A. Cliffe, M. B. Giles, R. Scheichl, and A. L. Teckentrup, "Multilevel Monte Carlo methods and applications to elliptic PDEs with random coefficients," *Comput. Visual Sci.*, **14**, 3, pp. 3–15, 2011.

[13] F. Kojima, ,"Stochastic inversion for electromagnetic propagation in a dielectric medium using Hamiltonian Monte Carlo method," in *47th ISCIE International Symposium on Stochastic Systems Theory and Its Applications*, Honolulu, HI, US, 2015.

[14] L. Hebert, T. Holzer, T. Eveleigh, and S. Shahryar, "Use of multifidelity and surrogate models in the design and development of physics-based systems," *Systems Engineering* **19**, 4, 2016.

Chapter 3

Polynomial Approximation of Stochastic Field Variation

3.1 Introduction

Many techniques for uncertainty quantification in CEM model the stochastic field variation caused by uncertainties in material properties using polynomial expansions. The fields are represented as polynomial functions of the uncertain material properties (e.g. [1]–[10]). The coefficients of the polynomials are obtained using either a single stochastic CEM simulation or a small number of deterministic CEM simulations. Once the coefficients are obtained, the polynomial expansion is used to evaluate the mean and variance of the field quantities of interest.

The polynomial order of the expansion directly impacts the computational complexity of the CEM simulation. For example, we have previously shown that the polynomial order required to obtain accurate field means and variances using the polynomial chaos expansion (PCE) technique with the finite- difference time-domain (FDTD) method can be very small for some problems but extremely large for others [11]. Thus the computational cost of PCE-FDTD is highly variable, and in some cases prohibitively high. Furthermore, the necessary polynomial order to achieve sufficient accuracy is not known a priori. While this previous investigation provides important specific insights about the computational complexity of PCE-FDTD, it does not yield broadly applicable insights about the accuracy of polynomial approximations in general.

A fundamental question is whether polynomial functions yield adequate approximations of the relationship between uncertain material properties and field quantities. We decouple this underlying question from the confounding problem of accurately estimating the coefficients for a given expansion. We seek to assess the inherent approximation capability of polynomial approximations. This is achieved by investigating the accuracy with which polynomial model expansions of different orders capture the standard deviation of statistical variations in field values in three canonical scattering scenarios involving simple scatterers with dielectric uncertainties for which the exact field solution is well known. Use of known exact field solutions eliminates the effects of errors in polynomial coefficient estimation that result from using particular computational methods (e.g. PCE-FDTD). We determine the order required to achieve accurate

polynomial approximations of field value variations and show that many scenarios require too high of an order to be effective in practice. The existence of such cases in simple scattering scenarios suggest that great care must be exercised in using polynomial approximations of statistical field variations for uncertainty quantification in CEM.

The next section briefly describes the three scattering scenarios. Section 3.3 presents the investigation procedure. The last two sections detail the results and the conclusions. We use $\langle \cdot \rangle$ to denote the mean value and $\mathrm{s.d.}\,\{\cdot\}$ to denote standard deviation throughout this dissertation.

3.2 The Scattering Scenarios

We consider three canonical scattering scenarios involving uniform plane waves incident upon scatterers with dielectric uncertainties: a dielectric slab of finite thickness and infinite area, a dielectric circular cylinder of infinite length, and a dielectric sphere. The well-known analytical expressions for the electric field phasors at observation points outside the scatterer are used to benchmark the accuracy of the polynomial approximation.

3.2.1 Slab with uncertain dielectric properties

A dielectric slab of thickness equal to $2\lambda_0$, where λ_0 is the free-space wavelength, is illuminated by a uniform plane wave at normal incidence. Two observation planes are chosen, one in the backscatter region and the other in the forward scattering region. The electric fields in each of these planes are evaluated for varying values of the dielectric properties of the slab. The observation plane in the forward scattering region is considered in our analysis only if the magnitude of fields reaching this region is greater than 0.1% of the magnitude of the incident field.

3.2.2 Cylinder with uncertain dielectric properties

A dielectric circular cylinder of infinite length and cross-sectional radius equal to $\lambda_0/2$ is illuminated by a uniform plane wave at normal incidence with the electric field vector oriented parallel to the axis of the cylinder (i.e., the transverse magnetic scattering scenario). A set of observation lines at different azimuth angles is chosen at a constant radial distance of $9\lambda_0/10$ from the cylinder axis. The electric fields are evaluated for varying values of the dielectric properties of the cylinder.

3.2.3 Sphere with uncertain dielectric properties

A dielectric sphere of radius equal to $5\lambda_0/12$ is illuminated by a uniform plane wave. The observation points are chosen at different azimuth and polar angles at a constant radial distance of $5\lambda_0/8$ from the

center of the sphere. The electric fields at these observation points are evaluated for varying values of the dielectric properties of the sphere.

3.3 Investigation Procedure

We first consider uncertainty in the relative permittivity, ϵ_{r}, of the dielectric scatterer assuming fixed effective conductivity, σ. We choose a standard deviation for ϵ_{r} that is 2.5% of its mean value, $\langle \epsilon_{\mathrm{r}} \rangle$. We consider 100 scenarios of $\langle \epsilon_{\mathrm{r}} \rangle$ ranging from 1.3 to 80.5. This spans the range of $\langle \epsilon_{\mathrm{r}} \rangle$ values from that close to air all the way up to that of water. For each value of $\langle \epsilon_{\mathrm{r}} \rangle$, we consider 100 fixed values of σ in the range from 5 mS/m - nearly lossless - to 5000 mS/m - very lossy - at an operating frequency of 2 GHz.

The normalized electric field phasor at any observation position $\vec{r}_i$, denoted by $\boldsymbol{E}(\vec{r}_i)$, is obtained using the relevant analytical expression [12]. Here, the normalization factor is the magnitude of the incident field. For each of the 100×100 combinations of $\langle \epsilon_{\mathrm{r}} \rangle$ and σ of the dielectric scatterer, we estimate the mean and standard deviation of the magnitude of the normalized field phasor, $|\boldsymbol{E}(\vec{r}_i)|$, at each $\vec{r}_i$ by evaluating the following two integral expressions numerically:

$$\langle |\boldsymbol{E}(\vec{r}_i)| \rangle = \int |\boldsymbol{E}(\vec{r}_i, \epsilon_r)| \, p(\epsilon_{\mathrm{r}}) \, \mathrm{d}\epsilon_{\mathrm{r}} \tag{3.1}$$

$$\mathrm{s.d.}\{|\boldsymbol{E}(\vec{r}_i)|\} = \sqrt{\int \left(|\boldsymbol{E}(\vec{r}_i, \epsilon_{\mathrm{r}})| - \langle |\boldsymbol{E}(\vec{r}_i)| \rangle\right)^2 p(\epsilon_{\mathrm{r}}) \, \mathrm{d}\epsilon_{\mathrm{r}}} \tag{3.2}$$

Here, $p(\epsilon_{\mathrm{r}})$ represents the probability distribution of ϵ_{r}. In our investigation, we assume all uncertain dielectric parameters to have a normal distribution, as in [4]. Hence, $p(\epsilon_{\mathrm{r}})$ is expressed as follows:

$$p(\epsilon_{\mathrm{r}}) = \frac{1}{\sqrt{2\pi}\,(\mathrm{s.d.}\{\epsilon_{\mathrm{r}}\})} \exp\left(-\frac{(\epsilon_{\mathrm{r}} - \langle \epsilon_{\mathrm{r}} \rangle)^2}{2\,(\mathrm{s.d.}\{\,\epsilon_{\mathrm{r}}\,\})^2} \right) \tag{3.3}$$

For each of the 100×100 combinations of $\langle \epsilon_{\mathrm{r}} \rangle$ and σ of the dielectric scatterer and at each $\vec{r}_i$, we fit polynomial model expansions to the analytical expression for $\boldsymbol{E}(\vec{r}_i)$ over the range of variation of ϵ_{r} and denote the polynomial approximation as $\hat{\boldsymbol{E}}(\vec{r}_i, D)$, where D is the polynomial order. We consider orders ranging from 1 to 50. In this study we have chosen to use orthogonal polynomials, specifically Hermite polynomials with an orthogonalization weight function given by $p(\epsilon_{\mathrm{r}})$. The polynomial model approximation $\hat{\boldsymbol{E}}(\vec{r}_i, D)$ is expressed in terms of Hermite polynomials as follows:

$$\hat{\boldsymbol{E}}(\vec{r}_i, D) = \sum_{n=0}^{D} \chi_n \mathrm{H}_n\left(\frac{\epsilon_{\mathrm{r}} - \langle \epsilon_{\mathrm{r}} \rangle}{\sqrt{2}\,(\mathrm{s.d.}\{\,\epsilon_{\mathrm{r}}\,\})} \right) \tag{3.4}$$

where χ_n represents the n^{th} coefficient in the polynomial model approximation and $\mathrm{H}_n(\cdot)$ represents the n^{th} order Hermite polynomial. The n^{th} coefficient, χ_n, is obtained by numerically evaluating the following integral:

$$\chi_n = \frac{1}{||\mathrm{H}_n||_2} \int \boldsymbol{E}(\vec{r}_i, \epsilon_{\mathrm{r}})\, \mathrm{H}_n\!\left(\frac{\epsilon_{\mathrm{r}} - \langle \epsilon_{\mathrm{r}} \rangle}{\sqrt{2}\,(\mathrm{s.d.}\{\,\epsilon_{\mathrm{r}}\,\})} \right) p(\epsilon_{\mathrm{r}})\, \mathrm{d}\epsilon_{\mathrm{r}} \tag{3.5}$$

where $||\cdot||_2$ represents the ℓ^2-norm.

Each of the integrals in (3.1), (3.2) and (3.5) is computed numerically using a Riemann sum approximation. The number of terms required for a highly accurate approximation of the integral is determined via a convergence test. Specifically, the number of terms is successively doubled until the new result represents less than a 0.1% change in the approximation, at which point we conclude that convergence has been reached.

The estimated standard deviation of the magnitude of the approximated field phasor, $|\hat{\boldsymbol{E}}(\vec{r}_i, D)|$, is obtained for orders $D = 1$ to 50 using (3.2) and compared to the standard deviation of the magnitude of the exact field phasor at every $\vec{r}_i$ using the following error metric:

$$\mathrm{e}(D) = \max_{\vec{r}_i} \left\{ \frac{|\mathrm{s.d.}\{|\boldsymbol{E}(\vec{r}_i)|\} - \mathrm{s.d.}\{|\hat{\boldsymbol{E}}(\vec{r}_i, D)|\}|}{\langle |\boldsymbol{E}(\vec{r}_i)| \rangle} \right\} \tag{3.6}$$

This error metric represents the maximum difference between the actual and approximated standard deviations expressed as a fraction of the mean value of the magnitude of the field phasor. Here, the maximum is taken over all observation points $\vec{r}_i$.

We define $D_{\min}$ as the minimum order for which the error metric is less than 0.01 or 1%. The values of $D_{\min}$ for all the 100×100 combinations of $\langle \epsilon_{\mathrm{r}} \rangle$ and σ are determined for each dielectric scatterer. The procedure is repeated for the case of 5.0% uncertainty in ϵ_{r} and each fixed σ.

Next, the analysis is repeated for 2.5% and 5.0% uncertainties in σ while ϵ_{r} is held fixed.

3.4 Results and Discussion

Figure 3.1(a) and (b) depicts $D_{\min}$ for 2.5% and 5% uncertainty, respectively, in ϵ_{r}, for the dielectric slab scenario. The required polynomial order varies widely from 1 to greater than 50. We see similar results for the dielectric cylinder scenario and the dielectric sphere scenario with uncertain ϵ_{r} as shown in Figures 3.2 and 3.3. It is not surprising to see that accurately approximating the functional dependence of the field on ϵ_{r} requires a very high order polynomial expansion in certain instances, given that the analytical expressions for the field values involve infinite series of Bessel functions (in the case of the cylinder) and spherical Bessel functions (in the case of the sphere) [12].

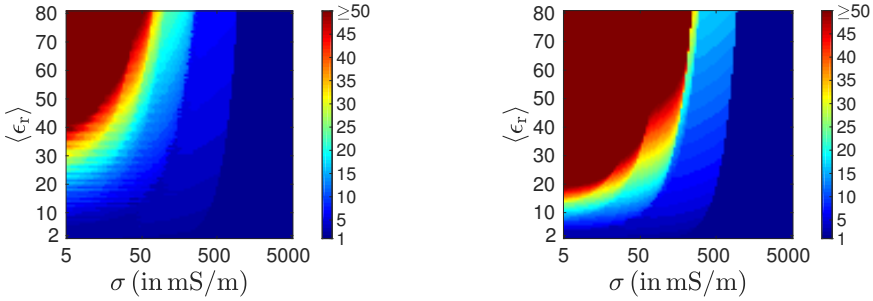

(a) (b)

Figure 3.1: Color images of $D_{\min}$ for dielectric slabs with known σ and uncertain ϵ_r. (a) 2.5% uncertainty, (b) 5% uncertainty in ϵ_r of the slab.

The plots in Figure 3.4 provide insights as to why the polynomial order necessary for an accurate approximation of the field dependence on ϵ_r of sphere is so highly variable. Figure 3.4(a) shows the variation of the electric field phasor magnitude (at 2 GHz) at a single observation point located outside the dielectric sphere as a function of ϵ_r with fixed σ = 12.5 mS/m. The field phasor is observed at a polar angle of $45°$ and an azimuth of $0°$ with respect to the direction of plane wave incidence. The complicated field variation is attributed to the complex interplay between constructive and destructive wave interference that takes place within and around the sphere as the electrical size of the sphere increases.

The minimum required polynomial order for accurately representing the variation in electric field outside the dielectric sphere, for a 2.5% uncertainty in ϵ_r, is plotted in Figure 3.4(b) as a function of $\langle \epsilon_r \rangle$. For small values of $\langle \epsilon_r \rangle$, an uncertainty of 2.5% does not cover any regions of significant field variations seen in Figure 3.4(a). For example, a standard deviation of 2.5% around a mean of 10 corresponds to only 0.25 units of relative permittivity – a very small range over which the field variation is not dramatic. Hence, the field variation can be accurately approximated using relatively low order polynomial expansions in this regime. However, for large values of $\langle \epsilon_r \rangle$, an uncertainty of 2.5% is large enough to cover regions of significant field variations seen in Figure 3.4(a). Hence, the field variation in this regime can only be accurately approximated using polynomial expansions of very high order.

We found $D_{\min} = 1$ for all considered cases of uncertain σ and fixed ϵ_r and for all three types of scatterers. Hence, we are not showing the corresponding figures. The utility of a polynomial expansion of first order indicates that the fields vary linearly with uncertain σ in these scenarios.

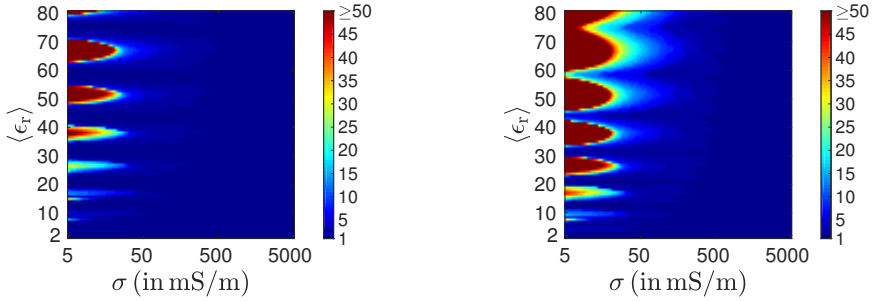

(a) (b)

Figure 3.2: Color images of $D_{\min}$ for dielectric cylinders with known σ and uncertain ϵ_r. (a) 2.5% uncertainty, (b) 5% uncertainty in ϵ_r of the cylinder.

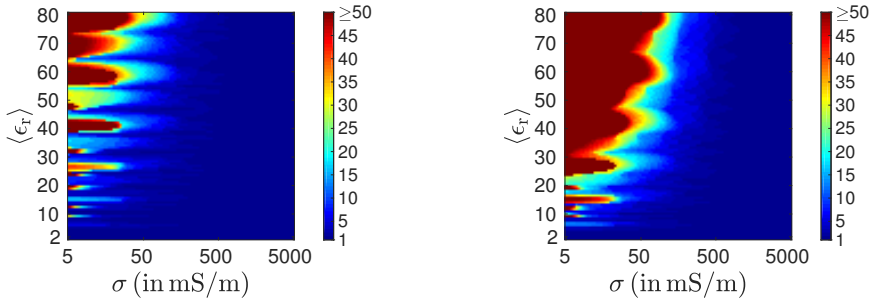

(a) (b)

Figure 3.3: Color images of $D_{\min}$ for dielectric spheres with known σ and uncertain ϵ_r. (a) 2.5% uncertainty, (b) 5% uncertainty in ϵ_r of the sphere.

3.5 Conclusions

This investigation has demonstrated two key points. First, the accuracy of polynomial approximations of field variations varies significantly with mean dielectric properties for canonical scattering scenarios. Lower-order polynomial expansions are sufficient for cases where the field variation is not significant over the range of uncertainty in dielectric properties, while higher-order polynomial expansions are required for cases where the field variation with dielectric properties is significant over the range of uncertainty. In fact, it is not uncommon for the required polynomial order to exceed what is practical from a computational point of view in these simplest scattering scenarios. Second, the applicability of such polynomial approximations to a given canonical scattering problem involving dielectric uncertainties and, by extension, to uncertainty quantification problems involving more complicated scatterers that exhibit dielectric

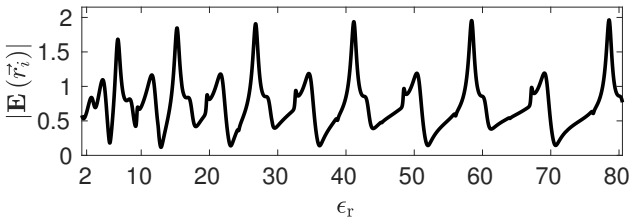

(a)

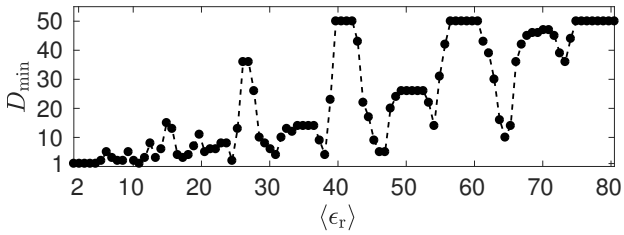

(b)

Figure 3.4: A dielectric sphere of radius = $5\lambda_0/12$ and σ = 12.5 mS/m is illuminated by a uniform plane wave. The electric field phasor at f = 2 GHz is observed at a point $\vec{r}_i$ located at $5\lambda_0/8$ from the center of sphere and at a polar angle of $45°$ and an azimuth of $0°$ with respect to the direction of plane wave incidence. (a) Magnitude of the observed field phasor as a function of ϵ_r. (b) $D_{\min}$ as a function of $\langle\epsilon_r\rangle$ assuming 2.5% uncertainty in ϵ_r of the sphere.

uncertainties, cannot be determined *a priori*. One proposed approach [8] for addressing these computational challenges involves dividing the domain of field variation into subdomains adaptively until low-order polynomial approximations are accurate in each of the subdomains. However, there is no evidence to date suggesting that such strategies reduce the computational cost to practical levels for a wide range of uncertainty quantification problems in CEM.

3.6 References

[1] C. D. Sarris and H. D. Lang, "Broadband sensitivity analysis in a single FDTD simulation with the complex step derivative approximation," in *2015 IEEE MTT-S Int. Microw. Symp.*, Phoenix, AZ, 2015, pp. 1–3.

[2] T. T. Zygiridis, N. V. Kantartzis, and T. D. Tsiboukis, "Investigation of uncertainty in lightning-produced EM Fields with a polynomial-chaos FDTD approach," *Int. J. Numer. Model.*, 2017; e2238.

[3] C. Chauviere, J. S. Hesthaven, and L. Lurati, "Computational modeling of uncertainty in time-domain electromagnetics," *SIAM J. Sci. Comput.*, vol. 28, no. 2, pp. 751–755, 2006.

[4] R. S. Edwards, A. C. Marvin, and S. J. Porter, "Uncertainty analyses in the finite-difference time-domain method," *IEEE Trans. Electromagn. Compat.*, vol. 52, no. 1, pp. 155–163, February 2010.

[5] A. C. M. Austin, N. Sood, J. Siu, and C. D. Sarris, "Application of polynomial chaos to quantify uncertainty in deterministic channel models," *IEEE Trans. Antennas Propag.*, vol. 61, no. 11, pp. 5754–5761, 2013.

[6] M. L. Gilbert and F. L. Teixeira, "A small-perturbation automatic-differentiation method for determining uncertainty in computational electromagnetics," *IEEE Trans. Antennas Propag.*, vol. 60, no. 11, pp. 5305–5314, 2012.

[7] A. Narayan and D. Xiu, "Stochastic collocation methods on unstructured grids in high dimensions via interpolation," *SIAM J. Sci. Comput.*, vol. 34, no. 3, pp. 1729–1752, 2012.

[8] A. C. Yücel, H. Bagcı, and E. Michielssen, "An adaptive multi-element probabilistic collocation method for statistical EMC/EMI characterization," *IEEE Trans. Electromagn. Compat.*, vol. 55, no. 6, pp. 1154–1168, December 2013.

[9] L. J. Gomez, A. C. Yücel, L. Hernandez-Garcia, S. F. Taylor, and E. Michielssen, "Uncertainty quantification in transcranial magnetic stimulation via high-dimensional model representation," *IEEE Trans. Biomed. Eng.*, vol. 62, no. 1, pp. 361–372, January 2015.

[10] J. S. Ochoa and A. C. Cangellaris, "Macro-modeling of electromagnetic domains exhibiting geometric and material uncertainty," *Applied Computational Electromagnetics Society Journal*, vol. 27, no. 2, pp. 80–87, 2012.

[11] S. Ganta, B. D. Van Veen, and S. C. Hagness, "On the computational complexity of polynomial chaos expansion for FDTD-based uncertainty analyses," in *2015 North American Radio Science Meeting*, Vancouver, BC, Canada, 2015.

[12] C. A. Balanis, *Advanced Engineering Electromagnetics*, 2nd ed., Hoboken, NJ, USA: Wiley, 2012.

Chapter 4

Sensitivity Analysis using Electric Field Integral Equations (EFIE)

4.1 Introduction

The most commonly used deterministic CEM techniques are the Finite Difference Time-Domain (FDTD) method [1], Finite-Element Method (FEM) [2] and Method of Moments (MoM) [3]. However, the various properties of the scatterers, sources and receivers cannot be known deterministically either due to the limitations of current measurement techniques or due to the fact that these properties are dynamically changing depending on the surrounding ambient conditions of temperature, pressure and humidity. Quantifying the uncertainty resulting in the fields [4] due to uncertainties of low magnitude in material and geometric properties is called sensitivity analysis. Sensitivity analysis of field values with respect to uncertainties in the various properties of scatterers, sources and receivers, if done with low computational cost, can be of great help in improving the computational efficiency and accuracy of such uncertainty quantification.

In problems involving antenna design [5], calibration of sensing antennas [12] and inverse scattering [6], we need to tweak the properties of sources, scatterers and receivers in order to get a desired field output. It is advantageous to have a method to evaluate the sensitivity of field output towards these properties. This would help in accelerating the procedure used to solve design optimization problems, system calibration problems or the inverse-scattering imaging problems if the sensitivity analysis method employed is of low computational cost.

In sensitivity analysis, each property of scatterers, sources and receivers on which the field values depend is termed as sensitivity parameter or simply a parameter. The sensitivity analysis can be local or global. Local sensitivity analysis is that which is relevant over an infinitesimally small neighborhood region around a chosen point in the multi-dimensional space spanned by the parameters. Global sensitivity analysis is that which is relevant over a relatively larger region in the multi-dimensional space spanned by the parameters covering all the plausible values that each parameter can take according to the problem

at hand. Both local and global sensitivity analysis techniques can be effectively used to improve computational efficiency of various design optimization problems and uncertainty quantification problems. We propose a new local sensitivity analysis technique in this dissertation.

Local sensitivity analysis requires estimating the gradient of field values at a chosen point. Estimating the gradient involves estimating derivatives of field values with respect to every parameter. Let $\{\xi_1, \xi_2, ..., \xi_N\}$ represent N parameters in a local sensitivity analysis problem and let $X(\xi_1, \xi_2, ..., \xi_N)$ represent a field value in the problem. The field value is denoted here as a function of all the N parameters. The gradient of the field value X can be written as:

$$\nabla X(\ldots, \xi_i, \ldots) = \sum_{i=1}^{N} \frac{\partial X(\ldots, \xi_i, \ldots)}{\partial \xi_i} \, \hat{\xi}_i \tag{4.1}$$

Here, $\hat{\xi}_i$ represents a unit vector in the dimension represented by the i^{th} parameter ξ_i. Each of the N derivative terms in equation (4.1) have to be estimated that form the gradient.

Let $\{\xi_1^0, \xi_2^0, \ldots, \xi_N^0\}$ represent the chosen point in the multi-dimensional parameter space. We need to estimate the gradient at that point, $\nabla X(\ldots, \xi_i, \ldots)\big|_{\{\ldots,\xi_i,\ldots\}=\{\ldots,\xi_i^0,\ldots\}}$. The estimation of this gradient involves estimating the derivatives, $\frac{\partial X(\ldots,\xi_i,\ldots)}{\partial \xi_i}\Big|_{\xi_i=\xi_i^0}$.

The most commonly used derivative estimation technique in the realm of CEM simulations is difference approximation [7]. Field values are recorded in this technique using deterministic CEM simulations before and after introducing a small perturbation in the parameter with respect to which the derivative to be estimated is defined. The difference in the field values recorded before and after the perturbation is divided by the magnitude of perturbation introduced in the parameter to get an estimate of the derivative. Let Δ_i be the magnitude of perturbation added to the i^{th} parameter at the point ξ_i^0. The difference approximation of the derivative of field value, $X(\ldots, \xi_i, \ldots)$, with respect to parameter ξ_i at the point ξ_i^0 can be written as:

$$\left.\frac{\partial X(\ldots, \xi_i, \ldots)}{\partial \xi_i}\right|_{\xi_i=\xi_i^0} \approx \frac{X(\ldots, \xi_i^0 + \Delta_i, \ldots) - X(\ldots, \xi_i^0, \ldots)}{\Delta_i} \tag{4.2}$$

Difference approximation of derivative obtained using an arbitrary value of magnitude of perturbation may not be accurate. Let $\tilde{\Delta}_i$ be the scaled magnitude of perturbation introduced in the i^{th} parameter where $\tilde{\Delta}_i = \Delta_i / \xi_i^0$. Too small a magnitude of $\tilde{\Delta}_i$ may cause the accuracy of the corresponding derivative estimate to be bogged down by numerical errors that may have crept into field values while using CEM simulations to obtain them. Too high a magnitude of $\tilde{\Delta}_i$ may cause the accuracy of the corresponding derivative estimate to be bogged down by the plausible non-linearity of field variation with respect to the i^{th} parameter near the chosen point. The accuracy is not affected only if the field value varies linearly with respect to ξ_i in the range from ξ_i^0 to $\xi_i^0 + \Delta_i$ since the difference approximation is a linear approximation technique. So,

a convergence test is required to arrive at a favorable value of magnitude of perturbation, $\tilde{\Delta}_i$, for which the difference approximation of derivative will be accurate. Multiple CEM simulations may be required for recording fields corresponding to multiple values of the magnitude of perturbation during the convergence test thereby increasing the cost of the procedure. Also, the required computational load for the difference approximation technique scales with the number of parameters which makes the technique disadvantageous when the total number of sensitivity parameters is very high. The required computational load for other existing derivative estimation techniques like auto-differentiation [8] also scales with the number of parameters.

We present a new derivative estimation technique in this dissertation that uses the electric-field integral equations (EFIE). The technique is to be used towards estimating the gradient of field values which is in turn to be used for the local sensitivity analysis. The derivatives are represented as volume integrals using EFIE in this technique. The volume integrals are then evaluated using discrete Riemann sum approximations where the field values and spatial gridding necessary for the discrete Riemann sum approximation are obtained from deterministic CEM simulations. This new technique does not require any perturbation and, as a result, does not require any convergence test. Accuracy of the derivative estimate increases with the increase in spatial grid resolution and hence, using a good resolution in deterministic CEM simulations guarantees an accurate estimate. The cost of EFIE method does not scale with the number of parameters but it does scale with the number of observation points at which gradients of field values are to be estimated. Hence, this new method is suitable for problems with a large number of parameters and a small number of observation points.

The following section contains a detailed procedure of derivative estimation using EFIE. A scattering scenario involving the two-dimensional canonical cylindrical scatterer is used to compare the EFIE method with difference approximation method in Section 4.3. Here, the results of derivative estimation obtained using the two methods are measured against the known analytical solution of derivative of fields for this example so as to compare the accuracy of the two methods. Also, the computational cost of the two methods in this scattering example are compared in this section. In Section 4.4, we use the EFIE method in a two-dimensional photonic crystal waveguide branch [14] example. Here, we study the sensitivity of transmissivity in one of the outlets of the branch towards the radii of dielectric rods in the vicinity of the branch. The results of this study are discussed in section 4.5. The last two sections detail the conclusions and list the acknowledgements respectively.

4.2 Derivative estimation using EFIE

Consider a generic 3D scattering scenario where there are M homogeneous scattering regions with permittivities of ϵ_1, ..., ϵ_j, ..., ϵ_M and volumes of V_1, ..., V_j, ..., V_M for the M regions respectively. The background region is air with a permittivity of ϵ_0. All the scattering regions along with the background are considered to be non-magnetic or, in other words, they all have a permeability which is same as that of free space (μ_0). There is one observation point, $\vec{r}$, and one source point, $\vec{r}_0$. Let all the electric field phasors be recorded at an angular frequency, ω.

The Electric Field Integral Equation (EFIE) for the scattered electric field phasor, $\vec{E}^{\,\mathrm{s}}$, at observation point, $\vec{r}$, resulting from a small change of $\Delta\epsilon_j$ in the permittivity of the j^{th} homogeneous scatterer can be written as follows [9]:

$$\vec{E}^{\,\mathrm{s}}(\vec{r}\,|\,\vec{r}_0) = \vec{E}^{\,\mathrm{t}}(\vec{r}\,|\,\vec{r}_0) - \vec{E}^{\,\mathrm{i}}(\vec{r}\,|\,\vec{r}_0) = \omega^2\mu_0 \iiint \left[\bar{\mathbf{G}}^{\mathrm{b}}(\vec{r}\,'|\,\vec{r}) \cdot \vec{E}^{\,\mathrm{t}}(\vec{r}\,'|\,\vec{r}_0)\right] \Delta\epsilon_j \, \mathrm{d}V_j \tag{4.3}$$

Here, $\vec{E}^{\,\mathrm{t}}$ and $\vec{E}^{\,\mathrm{i}}$ represent the total and incident electric field phasors respectively. $\vec{E}^{\,\mathrm{s}}(\vec{r}\,|\,\vec{r}_0)$ represents the scattered field phasor at observation point, $\vec{r}$, due to a source at $\vec{r}_0$. Similarly, $\vec{E}^{\,\mathrm{t}}(\vec{r}\,'|\,\vec{r}_0)$ represents total field phasor at an arbitrary point, $\vec{r}\,'$, inside the j^{th} homogeneous scattering region due to a source at $\vec{r}_0$. $\bar{\mathbf{G}}^{\mathrm{b}}(\vec{r}\,'|\,\vec{r})$ represents the background dyadic Green's function at $\vec{r}\,'$ with respect to the observation point, $\vec{r}$. The operator $(\cdot)$ represents a dot product between the dyadic Green's function and the field phasor vector.

Let ϵ_j^0 be the chosen value of net permittivity of the j^{th} homogeneous scattering region at which the derivative of field phasor with respect to relative permittivity is to be estimated. Let us assume that the chosen value of relative permittivity of the region is $\epsilon_{\mathrm{r},j}^0$. Let us assume that the change in net permittivity of the region, $\Delta\epsilon_j$, is caused by a small perturbation Δ introduced in the relative permittivity of the region only. The change in the net permittivity of the region, $\Delta\epsilon_j$, can now be expressed as follows:

$$\Delta\epsilon_j = \epsilon_0\left(\epsilon_{\mathrm{r},j}^0 + \Delta\right) - \epsilon_0\epsilon_{\mathrm{r},j}^0 = \epsilon_0\Delta$$

The total field phasors at the observation point and at an arbitrary point, $\vec{r}\,'$, in the scattering region along with the incident field phasor at the observation point can now be expressed in a new form by incorporating the information of perturbation in relative permittivity as follows:

$$\vec{E}^{\,\mathrm{t}}(\vec{r}\,|\,\vec{r}_0) \to E(\vec{r}\,|\,\vec{r}_0)|_{\epsilon_{\mathrm{r},j}=\epsilon_{\mathrm{r},j}^0+\Delta}$$

$$\vec{E}^{\,\mathrm{t}}(\vec{r}\,'|\,\vec{r}_0) \to E(\vec{r}\,'|\,\vec{r}_0)|_{\epsilon_{\mathrm{r},j}=\epsilon_{\mathrm{r},j}^0+\Delta}$$

$$\vec{E}^{\,\mathrm{i}}(\vec{r}\,|\,\vec{r}_0) \to E(\vec{r}\,|\,\vec{r}_0)|_{\epsilon_{\mathrm{r},j}=\epsilon_{\mathrm{r},j}^0}$$

Therefore, using these new forms for the field phasors, the EFIE in (4.3) can be rewritten as follows:

$$\vec{E}(\vec{r}\,|\,\vec{r}_0)\big|_{\epsilon_{\mathrm{r},j}=\epsilon^0_{\mathrm{r},j}+\Delta} - \vec{E}(\vec{r}\,|\,\vec{r}_0)\big|_{\epsilon_{\mathrm{r},j}=\epsilon^0_{\mathrm{r},j}} = \omega^2\mu_0\epsilon_0 \iiint \left[\bar{\mathbf{G}}^{\mathrm{b}}(\vec{r}\,'|\,\vec{r}) \cdot \vec{E}(\vec{r}\,'|\,\vec{r}_0)\big|_{\epsilon_{\mathrm{r},j}=\epsilon^0_{\mathrm{r},j}+\Delta}\right] \Delta \,\mathrm{d}V_j \tag{4.4}$$

Assuming a small perturbation in the relative permittivity of the j^{th} homogeneous scattering region (i.e., $\Delta \to 0$), we can apply the Born approximation [10] to the EFIE in (4.4). In other words, we can approximate field phasor $\vec{E}(\vec{r}\,'|\,\vec{r}_0)\big|_{\epsilon_{\mathrm{r},j}=\epsilon^0_{\mathrm{r},j}+\Delta}$ inside the integral with the field phasor $\vec{E}(\vec{r}\,'|\,\vec{r}_0)\big|_{\epsilon_{\mathrm{r},j}=\epsilon^0_{\mathrm{r},j}}$. With this approximation, the derivative of the field phasor $\vec{E}(\vec{r}\,|\,\vec{r}_0)$ with respect to the relative permittivity $\epsilon_{\mathrm{r},j}$ of the j^{th} homogeneous scattering region at the value $\epsilon^0_{\mathrm{r},j}$ can be expressed as follows:

$$\left.\frac{\partial \vec{E}(\vec{r}\,|\,\vec{r}_0)}{\partial \epsilon_{\mathrm{r},j}}\right|_{\epsilon_{\mathrm{r},j}=\epsilon^0_{\mathrm{r},j}} = \lim_{\Delta\to 0}\left[\frac{\vec{E}\big|_{\epsilon_{\mathrm{r},j}=\epsilon^0_{\mathrm{r},j}+\Delta} - \vec{E}\big|_{\epsilon_{\mathrm{r},j}=\epsilon^0_{\mathrm{r},j}}}{\Delta}\right] = \omega^2\mu_0\epsilon_0 \iiint \left[\bar{\mathbf{G}}^{\mathrm{b}}(\vec{r}\,'|\,\vec{r}) \cdot \vec{E}(\vec{r}\,'|\,\vec{r}_0)\big|_{\epsilon_{\mathrm{r},j}=\epsilon^0_{\mathrm{r},j}}\right] \mathrm{d}V_j \tag{4.5}$$

Using a similar procedure, we can obtain the derivative of the field phasor $\vec{E}(\vec{r}\,|\,\vec{r}_0)$ with respect to the conductivity σ_j of the j^{th} homogeneous scattering region at the value σ^0_j and express it as follows:

$$\left.\frac{\partial \vec{E}(\vec{r}\,|\,\vec{r}_0)}{\partial \sigma_j}\right|_{\sigma_j=\sigma^0_j} = \lim_{\Delta\to 0}\left[\frac{\vec{E}\big|_{\sigma_j=\sigma^0_j+\Delta} - \vec{E}\big|_{\sigma_j=\sigma^0_j}}{\Delta}\right] = -\mathrm{j}\omega\mu_0 \iiint \left[\bar{\mathbf{G}}^{\mathrm{b}}(\vec{r}\,'|\,\vec{r}) \cdot \vec{E}(\vec{r}\,'|\,\vec{r}_0)\big|_{\sigma_j=\sigma^0_j}\right] \mathrm{d}V_j \tag{4.6}$$

We notice that the integral expression for the derivative with respect to the conductivity σ_j of the j^{th} homogeneous scattering region is very similar in structure to the expression for the derivative with respect to relative permittivity $\epsilon_{\mathrm{r},j}$ of the region. The only difference is in the constant multiplication factor. We also notice from equations (4.5) and (4.6) that the derivative with respect to any dielectric property of a particular homogeneous scattering region depends only on fields recorded inside that homogeneous scattering region.

The electric field phasor inside the integral in equations (4.5) and (4.6), $\vec{E}(\vec{r}\,'|\,\vec{r}_0)$, can be expressed in terms of its cartesian components as follows:

$$\vec{E}(\vec{r}\,'|\,\vec{r}_0) = \begin{bmatrix} E_{\mathrm{x}}(\vec{r}\,'|\,\vec{r}_0) \\ E_{\mathrm{y}}(\vec{r}\,'|\,\vec{r}_0) \\ E_{\mathrm{z}}(\vec{r}\,'|\,\vec{r}_0) \end{bmatrix}$$

The background dyadic Green's function $\bar{\mathbf{G}}^{\mathrm{b}}(\vec{r}\,'|\,\vec{r}\,)$ at the point $\vec{r}\,'$ inside the j^{th} homogeneous scattering region can be expressed in terms of the field phasors $\vec{E}(\vec{r}\,'|\,\vec{r}\,)\big|_{\epsilon_{\mathrm{r},j}=\epsilon^0_{\mathrm{r},j}}$ recorded inside the scattering region

when a dipole current source of length L is placed at observation point $\vec{r}$ instead of source point $\vec{r}_0$ [10] as follows:

$$\bar{\mathbf{G}}^{\mathrm{b}}(\vec{r}\,'|\vec{r}) = \left(\frac{\mathrm{j}}{\omega\mu_0 L}\right)\cdot\begin{bmatrix} \frac{1}{I_{\mathrm{x}}}E_{\mathrm{x}}(\vec{r}\,'|\vec{r})\Big|_{I_y,I_z=0} & \frac{1}{I_{\mathrm{x}}}E_{\mathrm{y}}(\vec{r}\,'|\vec{r})\Big|_{I_y,I_z=0} & \frac{1}{I_{\mathrm{x}}}E_{\mathrm{z}}(\vec{r}\,'|\vec{r})\Big|_{I_y,I_z=0} \\ \frac{1}{I_{\mathrm{y}}}E_{\mathrm{x}}(\vec{r}\,'|\vec{r})\Big|_{I_z,I_x=0} & \frac{1}{I_{\mathrm{y}}}E_{\mathrm{y}}(\vec{r}\,'|\vec{r})\Big|_{I_z,I_x=0} & \frac{1}{I_{\mathrm{y}}}E_{\mathrm{z}}(\vec{r}\,'|\vec{r})\Big|_{I_z,I_x=0} \\ \frac{1}{I_{\mathrm{z}}}E_{\mathrm{x}}(\vec{r}\,'|\vec{r})\Big|_{I_x,I_y=0} & \frac{1}{I_{\mathrm{z}}}E_{\mathrm{y}}(\vec{r}\,'|\vec{r})\Big|_{I_x,I_y=0} & \frac{1}{I_{\mathrm{z}}}E_{\mathrm{z}}(\vec{r}\,'|\vec{r})\Big|_{I_x,I_y=0} \end{bmatrix} \tag{4.7}$$

Here, I_{x}, I_{y} and I_{z} are the currents in the dipole current source of length L placed at $\vec{r}$ when the dipole is oriented along x, y and z directions respectively. The field phasor components $E_{\mathrm{x}}(\vec{r}\,'|\vec{r})$, $E_{\mathrm{y}}(\vec{r}\,'|\vec{r})$ and $E_{\mathrm{z}}(\vec{r}\,'|\vec{r})$ are recorded in the scattering region for each of these dipole orientations when there is no perturbation in the relative permittivity in the region i.e., $\epsilon_{\mathrm{r},j} = \epsilon^0_{\mathrm{r},j}$.

The electric fields in (4.7) are obtained using a deterministic CEM simulation. So, a separate deterministic CEM simulation is needed for every dipole orientation at every observation point, $\vec{r}$, to obtain corresponding field phasors. However, we can obtain derivatives of a field phasor component at an observation point, $\vec{r}$, with respect to dielectric properties of all the M homogeneous scatterers using the field data obtained from just two CEM simulations, one with the source placed at the source point and the other with a dipole current source placed at the observation point respectively. Here, the dipole current source placed at the observation point should be oriented in the same direction as the component of field phasor at the observation point whose derivative we intend to estimate. Therefore, we can conclude that the cost of this EFIE based sensitivity analysis does not scale with the number of sensitivity parameters but does scale with the number of observation points and also with the number of phasor components at each observation point whose derivatives have to be estimated.

Let us assume we only intend to estimate the derivatives of z components of field phasor in equations (4.5) and (4.6). The field data and the spatial gridding used in the two required deterministic CEM simulations can be used to evaluate the integrals mentioned in equations (4.5) and (4.6) using discrete Riemann sum approximations. Their discrete forms are as follows:

$$\left.\frac{\partial E_{\mathrm{z}}(\vec{r}\,|\,\vec{r}_0)}{\partial \epsilon_{\mathrm{r},j}}\right|_{\epsilon_{\mathrm{r},j}=\epsilon^0_{\mathrm{r},j}} \approx \frac{\mathrm{j}\omega\epsilon_0}{L}\sum_{\vec{r}\,'}\left[\bar{\mathbf{G}}^{\mathrm{b}}(\vec{r}\,'|\vec{r})\cdot\vec{E}(\vec{r}\,'|\vec{r}_0)\big|_{\epsilon_{\mathrm{r},j}=\epsilon^0_{\mathrm{r},j}}\right]_{\mathrm{z}}\Delta v_j(\vec{r}\,') \tag{4.8}$$

$$\left.\frac{\partial E_{\mathrm{z}}(\vec{r}\,|\,\vec{r}_0)}{\partial \sigma_j}\right|_{\sigma=\sigma^0_j} \approx \frac{1}{L}\sum_{\vec{r}\,'}\left[\bar{\mathbf{G}}^{\mathrm{b}}(\vec{r}\,'|\vec{r})\cdot\vec{E}(\vec{r}\,'|\vec{r}_0)\big|_{\sigma_j=\sigma^0_j}\right]_{\mathrm{z}}\Delta v_j(\vec{r}\,') \tag{4.9}$$

Here, $\Delta v_j(\vec{r}\,')$ represents the volume of the discrete grid-unit (voxel) at position $\vec{r}\,'$ inside the volume of the j^{th} homogeneous scatterer of volume V_j. The subscript z used for the dot product of the dyadic background Green's function and electric field phasor vector in the R.H.S of the equations above represents the z component of the dot product.

In most cases, the spatial gridding is dense to ensure high accuracy of field values obtained in deterministic CEM simulations. Hence, there is little loss of accuracy by using these Riemann sum approximations to solve the integrals. It should also be noted that the field values in the integral can be obtained using any CEM simulation technique like FDTD, FEM and MoM. However, we have used the FDTD method [1] to obtain all the results shown in this dissertation.

4.3 EFIE-based derivative estimation in a canonical scattering problem

Consider the canonical scattering scenario of an infinitely long dielectric cylindrical scatterer with a single source and a single observation position in the back-scatterer region. The scatterer has a radius a, relative permittivity ϵ_{r} and conductivity σ.

Let us assume the cylindrical scatterer is oriented along the z direction. Now, we move from the three-dimensional full wave to the two-dimensional transverse magnetic (TM_{z}) polarization where only z components of electric fields are non-zero and where there can only be current sources oriented in z direction. The background dyadic Green's function in (4.7) can be simplified as follows:

$$\bar{\mathbf{G}}^{\text{b}}(\vec{r}\,'|\,\vec{r}) = \left(\frac{\text{j}}{\omega\mu_0 L I_{\text{z}}}\right) E_{\text{z}}(\vec{r}\,'|\,\vec{r})$$

Using the procedure that led to the development of equations (4.5) and (4.6), we can obtain expressions for derivatives of field value (z component of electric field phasor) at observation position with respect to ϵ_{r} and σ of scatterer at the values ϵ_{r}^0 and σ^0 respectively as follows:

$$\left.\frac{\partial E_{\text{z}}(\rho,\phi\,|\,\rho_0,\phi_0)}{\partial \epsilon_{\text{r}}}\right|_{\epsilon_{\text{r}}=\epsilon_{\text{r}}^0} = \omega^2\mu_0\epsilon_0 \iint E_{\text{z}}(\rho',\phi'\,|\,\rho,\phi)|_{\epsilon_{\text{r}}=\epsilon_{\text{r}}^0} E_{\text{z}}(\rho',\phi'\,|\,\rho_0,\phi_0)|_{\epsilon_{\text{r}}=\epsilon_{\text{r}}^0}\,\text{d}S \tag{4.10}$$

$$\left.\frac{\partial E_{\text{z}}(\rho,\phi\,|\,\rho_0,\phi_0)}{\partial \sigma}\right|_{\sigma=\sigma^0} = -\text{j}\omega\mu_0 \iint E_{\text{z}}(\rho',\phi'\,|\,\rho,\phi)|_{\sigma=\sigma^0} E_{\text{z}}(\rho',\phi'\,|\,\rho_0,\phi_0)|_{\sigma=\sigma^0}\,\text{d}S \tag{4.11}$$

We observe that the integrals in the EFIEs given in equations (4.10) and (4.11) are two-dimensional integrals reflecting the fact that we are dealing with a two-dimensional scattering scenario. We can solve these two two-dimensional integrals by evaluating their discrete Riemann sum approximations like the ones shown in equations (4.8) and (4.9) of the previous section.

We can demonstrate how the EFIE-based sensitivity analysis technique can be used to obtain derivatives of field values with respect to dimensions of dielectric scatterers using this canonical scattering example. Here, let us try to evaluate derivative of field value $E_z(\rho, \phi \,|\, \rho_0, \phi_0)$ with respect to variation in radius a of scatterer. Let there be a small perturbation of Δ ($\Delta \to 0$) in the radius at a value a^0. Now, the region of infinitesimal cross-sectional area between the concentric circles of radius a^0 and $a^0 + \Delta$ is the region whose dielectric properties change or, in other words, the region over which the EFIE is to be formulated. The change in the dielectric properties is just the difference between total permittivity of scatterer and that of air as the medium in this region changes from air to the scatterer as a result of the perturbation in radius. So, the change in permittivity can be expressed as follows:

$$\Delta\epsilon = \epsilon_0 \left(\epsilon_{\mathrm{r}} - 1.0 + \frac{\sigma}{\mathrm{j}\omega\epsilon_0} \right)$$

Let us use the cylindrical coordinate system to evaluate the area element $\mathrm{d}S$ in the region where EFIE is to be formulated. The value of cylindrical coordinate ρ' throughout the region of infinitesimal cross-sectional area can be approximated as a^0 since $\Delta \to 0$. Hence, using cylindrical coordinates, the area element $\mathrm{d}S$ can be written as:

$$\mathrm{d}S = \rho' \mathrm{d}\phi' = a^0 \Delta \mathrm{d}\phi'$$

Therefore, the EFIE to evaluate the derivative of field value with respect to radius can be written as follows:

$$\begin{aligned} &E_{\mathrm{z}}(\rho, \phi \,|\, \rho_0, \phi_0) \,|_{a=a^0+\Delta} - E_{\mathrm{z}}(\rho, \phi \,|\, \rho_0, \phi_0) \,|_{a=a^0} \\ &= \omega^2 \mu_0 \epsilon_0 \int \bar{\mathbf{G}}^{\mathrm{b}}(a^0, \phi' \,|\, \rho, \phi)\, E_{\mathrm{z}}(a^0, \phi' \,|\, \rho_0, \phi_0)|_{a=a^0} \left(\epsilon_{\mathrm{r}} - 1 + \frac{\sigma}{\mathrm{j}\omega\epsilon_0} \right) a^0 \mathrm{d}\phi' \end{aligned} \tag{4.12}$$

The derivative of field value $E_z(\rho, \phi \,|\, \rho_0, \phi_0)$ at the observation point with respect to radius a of the scatterer at the value a^0 can be then be expressed as follows:

$$\begin{aligned} &\left. \frac{\partial E_{\mathrm{z}}(\rho, \phi \,|\, \rho_0, \phi_0)}{\partial a} \right|_{a=a^0} = \lim_{\Delta \to 0} \left[\frac{E_{\mathrm{z}}(\rho, \phi \,|\, \rho_0, \phi_0)|_{a=a^0+\Delta} - E_{\mathrm{z}}(\rho, \phi \,|\, \rho_0, \phi_0)|_{a=a^0}}{\Delta} \right] \\ &= \omega^2 \mu_0 \epsilon_0 \int E_{\mathrm{z}}(a^{\mathrm{b}}, \phi' \,|\, \rho, \phi)|_{a=a^0} E_{\mathrm{z}}(a^{\mathrm{b}}, \phi' \,|\, \rho_0, \phi_0)|_{a=a^0} \left(\epsilon_{\mathrm{r}} - 1 + \frac{\sigma}{\mathrm{j}\omega\epsilon_0} \right) a^0 \mathrm{d}\phi' \end{aligned} \tag{4.13}$$

We observe in this EFIE that the integral is a 1D integral reflecting the fact that we are dealing with only one of the dimensions of the cylindrical scatterer i.e., the radius. We can solve this 1D integral by evaluating its discrete Riemann sum approximation similar to the ones seen in equations (4.8) and (4.9).

A similar EFIE-based methodology can be used to estimate derivatives of field values with respect to the multiple dimensions of more complexly-shaped scatterers like a polygon-shaped scatterer, where derivative with respect to one of its side is to be evaluated, for example. Also, similar methodologies can be used to estimate derivatives of field values with respect to various other parameters such as permeability of magnetic scatterers; shape/dimensions of metallic scatterers; and position/distance of any scatterer with respect to a fixed point in space.

4.4 Investigating accuracy of EFIE-based derivative estimation

Analytical field values and the analytical derivatives of field values are known in the canonical scattering scenario of an infinitely long dielectric cylindrical scatterer with a single source and a single observation position that was discussed in the previous sub-section. We can use these analytical solutions to determine and compare the accuracy of EFIE-based derivative estimation technique with that of difference approximation.

Consider a cylindrical scatterer of radius $a = \lambda_0/4$ where λ_0 represents the free-space wavelength. The source is at $(\rho_0, \phi_0) = (\lambda_0/2, 0)$ and the observation position is at $(\rho, \phi) = (3\lambda_0/4, 0)$ which is in the back-scatter region. The back scatter region is chosen because the variation in magnitude of field values is highest at this position for a range of different values of a, ϵ_r and σ of the scatterer. A two-dimensional TM_z polarization is assumed.

We chose 100 equally spaced values of permittivity, ϵ_r^0, of scatterer from 2 to 81.2. For each value of ϵ_r^0, we chose 100 values of loss tangent $\tan(\delta)$ of scatterer from 0.001 to 10.0. For each of these 100 x 100 (=10,000) combinations of ϵ_r^0 and $\tan(\delta)$ of scatterer, we computed analytical value of derivative of field at observation position with respect to ϵ_r and a of scatterer. We compared the magnitude of estimated derivative of the field value i.e., $\left|\frac{\partial E_z}{\partial \xi}\right|_{est.}$ (estimated either using EFIE method or difference approximation in the realm of FDTD simulations) to the analytical derivative $\left|\frac{\partial E_z}{\partial \xi}\right|$ using the following error metric:

$$\text{err} = \frac{\left|\left|\frac{\partial E_z}{\partial \xi}\right|_{est.} - \left|\frac{\partial E_z}{\partial \xi}\right|\right|}{\left|\frac{\partial E}{\partial \xi}\right|} \text{ (in \%)} \tag{4.14}$$

Here, ξ represents the uncertain parameter which can either be ϵ_r or a of scatterer. The error in magnitudes of the two derivatives with respect to both ϵ_r and a of scatterer were evaluated for both the EFIE-based

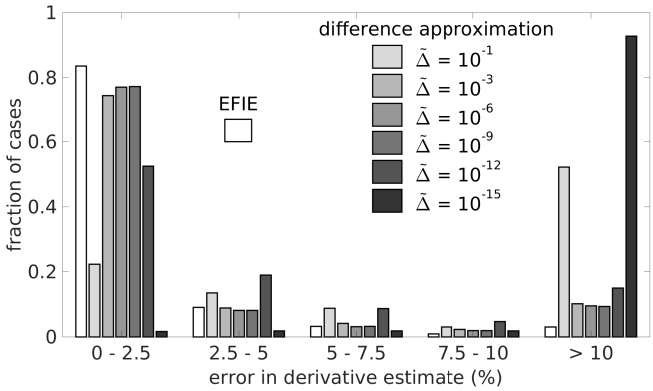

(a)

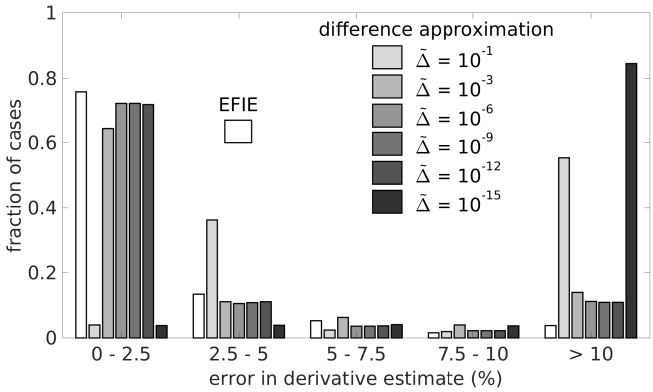

(b)

Figure 4.1: Histograms showing distribution of errors in the estimated magnitudes of derivatives of field value at a back-scatter observation position in a canonical cylindrical scattering scenario with respect to (a) relative permittivity, ϵ_r and (b) radius, a respectively of the cylindrical scatterer. The errors are evaluated for derivatives estimated using the EFIE method and also using the difference approximation method for different choices of scaled magnitude of perturbation in sensitivity parameter, $\tilde{\Delta}$. The error values are evaluated for 10,000 variations of the cylindrical scatterer with respect to its relative permittivity and loss tangent. The height of a bar in these histograms corresponding to any particular error bin represents the fraction of the 10,000 cases for which the error value in estimated derivative falls within the boundaries of the bin.

derivative estimation technique and the difference approximation technique. The error evaluation for difference approximation technique was repeated for multiple choices of the scaled magnitude of perturbation $\tilde{\Delta}$. Representative error bins (in %) were chosen and placed on x-axis of histogram plots. For each error bin, the number of cases where error falls in the range given in error bin was counted. The fraction of this number over 10,000 was marked using a bar placed against the respective error bin in the plots. The bars corresponding to both EFIE-based derivative estimation method and to the multiple choices of $\tilde{\Delta}$ in case of difference approximation technique were placed in the same plot. Figure 4.1(a) shows histogram

plot for errors in estimated magnitude of derivative with respect to ϵ_r of scatterer and Figure 4.1(b) shows histogram plot for errors in estimated magnitude of derivative with respect to a of scatterer respectively.

The error in magnitude of the EFIE derivative with respect to both ϵ_r and a of scatterer is low (<2.5%) for a larger number of cases compared to that of difference approximation for all choices of $\tilde{\Delta}$ considered. $\tilde{\Delta}$ is the scaled magnitude of perturbation in the sensitivity parameter given by $\tilde{\Delta} = \Delta/\epsilon_r^0$ or $\tilde{\Delta} = \Delta/a^0$ where Δ is the magnitude of perturbation in the parameter. There are some choices of $\tilde{\Delta}$ for which difference approximation error is high for almost all of 10,000 cases. There is no way of determining a good choice of $\tilde{\Delta}$ a priori. Also, the peak value of error in EFIE-based derivative estimate is below 100% in both the plots whereas the peak value of error in difference approximation based derivative estimate is considerably higher that 100% in both the plots.

4.5 Application

The EFIE derivative estimation can be used to calculate the derivative of field value at an observation point with respect to multiple sensitivity analysis parameters in an electromagnetic scenario. Each such derivative requires an EFIE integral formulation. However, all these formulated integrals can be evaluated by post processing field data from just two CEM simulations, one with source placed at the actual source position and another with source placed at the observation point. In other words, the cost of estimating a gradient of a field value at an observation point with respect to a vector of sensitivity analysis parameters does not scale with respect to the number of parameters in the vector. However, with every new observation point, one extra simulation is required with source placed at the new observation point. Therefore, suitable applications of the EFIE method with a small number of observation points and a large number of parameters include designing of 1D Bragg filter gratings [11], studying antenna systems for sensing applications [12], designing photonic devices such as Wavelength Division Multiplexers [13] etc. In two-dimensional photonic crystal waveguide branch [14], where the number of relevant observation points is low, EFIE-based derivative estimation can serve as a reliable and cost-effective tool for sensitivity analysis.

In the waveguide branch example, consider the radii of 105 rods in the proximity of the waveguide branch to be sensitivity parameters. The photonic crystals used in this waveguide branch have a band-gap in two-dimensional TM_z polarization. The transmissivity in one of the two branch outlets, measured as a % of maximum possible transmissivity of 0.5, is the physical quantity whose sensitivity with respect to the 105 parameters is analyzed. Let, d be the lattice constant of the crystal structure, ρ be the radius of crystals which are cylindrical dielectric rods ($\rho = 0.2d$) and let the frequency range of interest be $0.34c/d$ to $0.41c/d$ where c is the speed of light in vacuum. We first assume the 105 parameters to be varying simultaneously and not independently for simplicity. We estimate the change in transmissivity for a simultaneous change

of $\pm 1\%$ in the radii of all the 105 rods both by using an extra deterministic CEM simulation and by using linear interpolation with the help of EFIE-based derivative and then, we compare the two results. We then assume the 105 parameters to vary independently and obtain the 105 term gradient using the EFIE method. We estimate the change in transmissivity for a small change in the 105 parameters in the gradient descent direction both by using an extra CEM simulation and by using linear interpolation with the help of EFIE-based gradient and then, we compare the two results. Here, the change in the gradient descent direction of the 105 parameters is such that the maximum change in any of the 105 parameters is $\pm 1\%$.

In [14], two identical defect rods of undecided radius, ρ_{D}, are deliberately introduced at the entrance of the two outlets of the branch in order to increase the transmissivity to an optimum value of 100%. However, there is no procedure given in [14] to determine the radius, ρ_{D}, of the defect rods for which the transmissivity in the out channel will be optimum. We propose to determine this radius using the EFIE method. To begin, we use a generic initial guess of $0.05d$ for the radius of the two defect rods. We compute the transmissivity using a deterministic FDTD simulation and also obtain an EFIE-based derivative of transmissivity with respect to radius of the two defect rods. We then predict the value of radius, ρ_{D}, of the two rods for which transmissivity will be optimum using linear interpolation with the help of EFIE-based derivative. We run an extra deterministic FDTD simulation for this EFIE-predicted value of radius of the two rods and check if the transmissivity is indeed optimum at this radius.

4.6 Results and Discussion

In Figure 4.2(a), the diagram of the waveguide branch is shown with the 105 relevant rods in the proximity of the branch shown in gray unlike the remaining rods which are shown in black. The input and output channels are marked in this diagram. The transmissivity for a simultaneous change of $\pm 1\%$ in the radii of 105 rods is obtained using both extra deterministic FDTD simulations and linear interpolations using EFIE derivative and plotted in Figure 4.3 along with transmissivity for no change in radii (baseline). The results obtained using linear interpolations with EFIE derivative estimate and using extra simulations seem to be in agreement with each other.

The gradient of transmissivity with respect to the 105 parameters is obtained using the EFIE method. In Figure 4.4, the changed transmissivity for a small change in the radii of 105 rods in the gradient descent direction is obtained using both extra FDTD simulations and linear interpolations with EFIE gradient and plotted along with transmissivity for no change in radii (baseline). The change in the radii of 105 rods in the gradient descent direction is such that the maximum change in any of the 105 radii is $\pm 1\%$. The EFIE gradient interpolation result and the result obtained using extra simulation seem to be in agreement with each other.

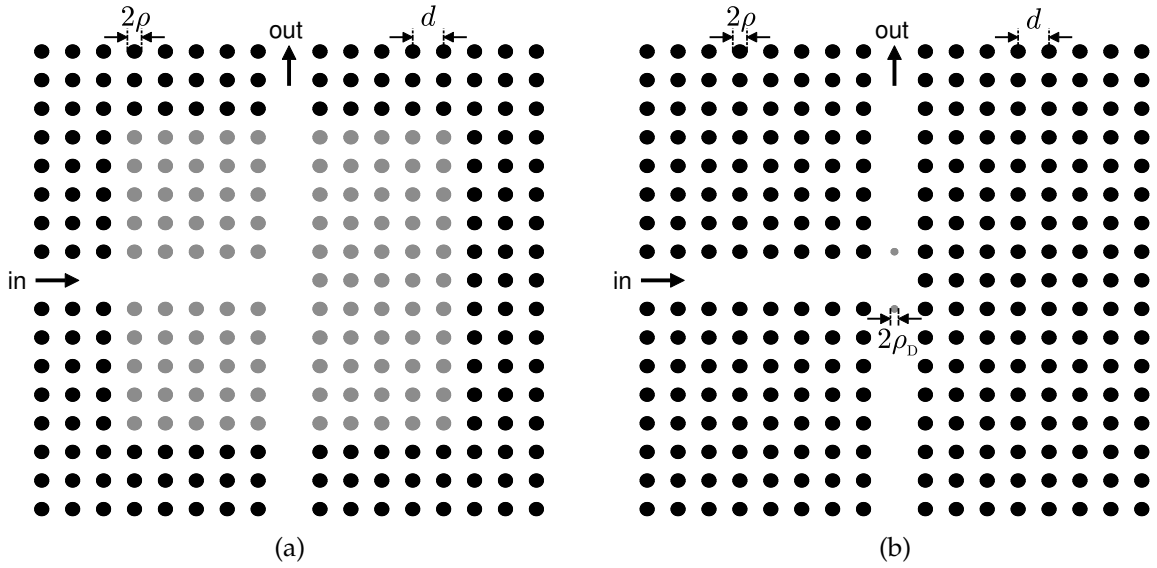

Figure 4.2: Diagrams of the two-dimensional photonic crystal waveguide branch showing the diameter of rods 2ρ and the lattice constant d along with the in and out channels. The 105 relevant rods in the vicinity of the branch whose radii affect the transmissivity in output channel most significantly are marked in gray in (a). Radii of these 105 rods are the sensitivity parameters in the problem. The two extra defect rods of undecided radius, ρ_{D} that are deliberately introduced in the waveguide branching region to improve the transmissivity in output channel to an optimum value are marked in gray in (b).

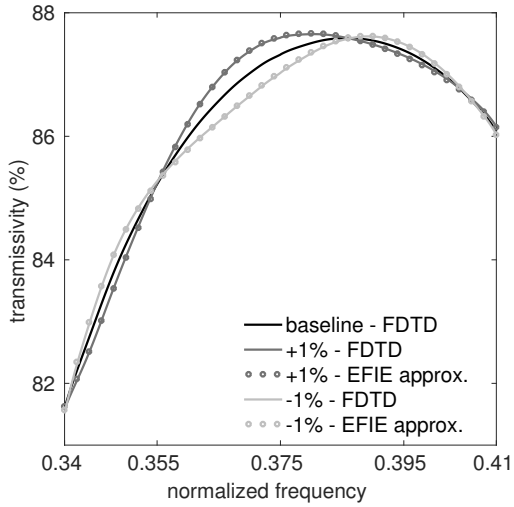

Figure 4.3: Transmissivity (measured as % of ideal transmissivity, 0.5) at the output channel of waveguide branch for unchanged radii of 105 rods is plotted (baseline) against normalized frequency. The results for transmissivity obtained using extra FDTD simulations and using linear interpolations with EFIE derivatives for simultaneous changes of +1% and -1% in radius of all the 105 relevant rods are also plotted.

In Figure 4.2(b), the diagram of the waveguide branch is shown with the two defect rods that are deliberately introduced in the two outlets of the waveguide branch to increase transmissivity to the maximum.

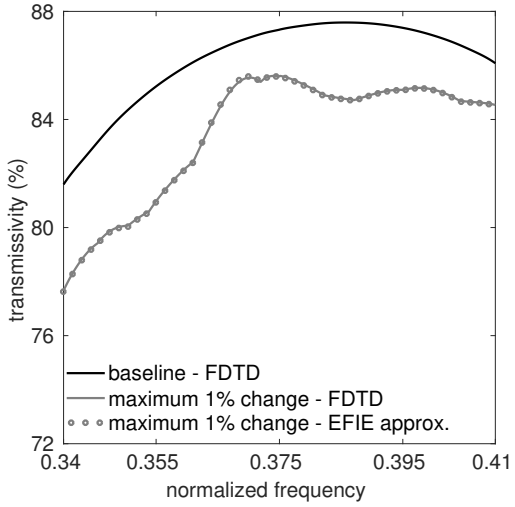

Figure 4.4: Transmissivity (measured as % of ideal transmissivity, 0.5) at the output channel of waveguide branch for unchanged radii of 105 rods is plotted (baseline) against normalized frequency. The gradient of transmissivity with respect to the 105 radii of rods is estimated using the EFIE method. The results for transmissivity obtained using extra FDTD simulations and using linear interpolations with EFIE gradient for a small change in the radii of 105 rods in the gradient descent direction are also plotted. The small change in radii of 105 rods in the gradient descent direction is such that the maximum change in any of the 105 values is $\pm 1\%$.

These are shown in gray unlike other rods that are in black. The transmissivity for no defect rods and for an initial guess of $0.05d$ for the radius, ρ_{D}, of the defect rods are plotted in Figure 4.5. The EFIE derivative of transmissivity with respect to radius of defect rods is evaluated. Using linear interpolation with help of the derivative, it is seen that at a value of $0.081d$ for the radius, ρ_{D}, of the rods, transmissivity reaches the optimum of 100% at a frequency of $0.41c/d$. This information is verified by running an extra FDTD simulation with the radius of rods having the predicted value of $0.081d$ and plotting the computed transmissivity in Figure 4.5. The transmissivity at a frequency of $0.41c/d$ is observed to be 99.99%. Hence, for this specific application, EFIE method proves to be both a good design optimization tool and an effective sensitivity analysis tool.

4.7 Conclusions

The required computational load for the EFIE-based sensitivity analysis method does not scale with the number of parameters. This puts the EFIE method at a very advantageous position to tackle problems where the number of sensitivity parameters is very high.

EFIE-based sensitivity analysis method provides an explicit expression for the derivative and hence, no convergence test is required as opposed to difference approximation-based sensitivity analysis. The extra

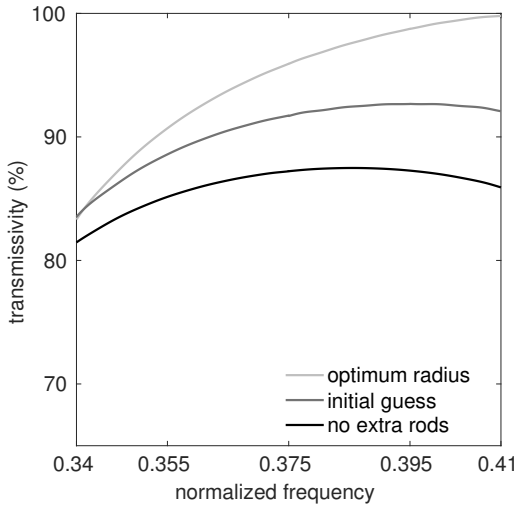

Figure 4.5: Transmissivity (measured as % of ideal transmissivity, 0.5) at the output channel of waveguide branch for no extra defect rods in the branch is plotted against normalized frequency. The transmissivity in the output channel for an initial guess of radius of $0.05d$ for the extra defect rods is also plotted. Also, the EFIE method predicts that optimum value of radius of extra defect rods for which transmissivity is 100% is $0.081d$ is plotted. Using an extra FDTD simulation, the transmissivity in the output channel for an optimum value of radius of $0.081d$ for the extra defect rods is also plotted.

computational cost involved in performing the convergence test is avoided making EFIE method more efficient computationally.

In the 10,000 variations of the canonical scattering problem involving the cylindrical scatterer, the derivatives estimated using EFIE-based sensitivity analysis method were observed to be more accurate on an average than the derivatives estimated using difference approximation method despite using a wide range of choices for the magnitude of difference or perturbation.

The required computational load for the EFIE-based sensitivity analysis method scales with the number of observation points and hence, cannot be used in applications with a large number of observation points. A classic example of such an application is the estimation of SAR (Specific Absorption Rate) [15].

A thorough comparison can be made between the adjoint sensitivity method and the EFIE method as future work in order to identify if the EFIE method has any specific advantages and/or limitations over the adjoint sensitivity method.

4.8 References

[1] A. Taflove, and S. C. Hagness, *Computational Electrodynamics: The Finite-Difference Time-Domain Method*, 3rd ed., Norwood, MA: Artech House, 2005.

[2] J. M. Jin, *The Finite Element Method in Electromagnetics*, 2nd ed., New York, NY: Wiley, 2002.

[3] W. C. Gibson, *The Method of Moments in Electromagnetics*, 2nd ed., Boca Raton, FL: CRC Press, 2015.

[4] M. A. Azpúrua, E. Páez, and R. Jauregui, "Measurement of uncertainty propagation through the feature selective validation method," in *2014 IEEE Int. Symp. on Electromag. Compat. (EMC)*, Raleigh, NC, 2014, pp. 328–333.

[5] C. A. Balanis, *Antenna Theory: Analysis and Design*, 3rd ed., Hoboken, NJ: Wiley, 2005.

[6] K. I. Hopcraft, and P. R. Smith, *An Introduction to Electromagnetic Inverse Scattering*, 1st ed., Netherlands: Springer, 1992.

[7] C. D. Sarris, and H. D. Lang, "Broadband sensitivity analysis in a single FDTD simulation with the complex step derivative approximation," in *2015 IEEE MTT-S Int. Microw. Symp.*, Phoenix, AZ, 2015, pp. 1–3.

[8] M. S. Gilbert, and F. L. Teixeira, "A small-perturbation automatic-differentiation method for determining uncertainty in computational electromagnetics," *IEEE Trans. Antennas Propag.*, vol. 60, no. 11, November 2012, pp. 5305–5314.

[9] W. C. Chew, *Waves and Fields in Inhomogeneous Media*, 1st ed., Piscataway, NJ: IEEE Press, 1995.

[10] T. J. Cui, Y. Qin, G. L. Wang, and W. C. Chew, "Low-frequency detection of two-dimensional buried objects using high-order extended Born approximations," *IOP Inverse Problems*, vol. 20, March 2004, pp. 41–62.

[11] B. P. Pal, S. Ghosh, R. K. Varshney, S. Dasgupta, and A. Ghatak, "Loss and dispersion tailoring in 1D photonics band gap Bragg reflection waveguides: finite chirped claddings as a design tool," *Opt. Quant. Electron.*, vol. 39, November 2007, pp. 983–993.

[12] S. Myllymaki, A. Huttunen, H. Jantunen, M. Berg, and E. Salonen, "Measurement method for sensitivity analysis of proximity sensor and sensor antenna integration in a handheld device," in *Progress*

in Electromagnetics Research C, vol. 20, 2011, pp. 255–268.

[13] V. Liu, Y. Jiao, D. A. B. Miller, and S. Fan, "Design methodology for compact photonic-crystal-based wavelength division multiplexers," *Optics Letters*, vol. 36, no. 4, February 2011.

[14] S. Fan, S. G. Johnson, J. D. Joannopoulos, C. Manolatou, and H. A. Haus, "Waveguide branches in photonic crystals," *J. Opt. Soc. Am. B*, vol. 18, no. 2, February 2001, pp. 162–165.

[15] E. Ofli, N. Chavannes, and N. Kuster, "The uncertainties and repeatability limitations of transmitter and receiver performance assessments posed by head phantoms," in *2006 IEEE Int. Workshop Antenna Technology Small Antennas Novel Metamaterials*, New York, March, 2006, pp. 349–352.

Chapter 5

Impact of Sampling Methods on Efficiency of Uncertainty Quantification

5.1 Introduction

There are inherent uncertainties in the measured properties of both naturally occurring and artificially engineered materials due to a variety of factors such as intrinsic heterogeneity, imperfections in measurement processes, and changing ambient conditions of temperature, pressure and humidity. Similarly, there are inherent uncertainties in the dimensions of fabricated devices and circuits due to manufacturing tolerances. These material and dimensional uncertainties translate to variability in the manner in which electromagnetic waves interact with such structures and ultimately impact the performance of the system.

Computational electromagnetics (CEM) simulations may be used to quantify the uncertainty in device performance due to material and dimensional uncertainties. Sampling-based uncertainty quantification methods use post-processing of computed field values corresponding to different sample values of the uncertain model parameters to estimate the statistical properties, for example, mean and standard deviation, of the output. In standard Monte Carlo methods [1], the samples are randomly chosen (e.g. [2]–[5]). Alternately, the samples may be deterministically chosen at pre-calculated quadrature points [6] for use in probabilistic collocation methods (e.g. [7]–[10]). The samples may follow the probability distribution of the stochastic model parameters or the samples may be uniformly distributed across the sample space.

In this dissertation, we evaluate the efficiency of random and deterministic sampling methods for uncertainty quantification in three representative CEM simulation examples. The first two examples are based on two-dimensional photonic crystal structures designed to operate as either a waveguide branch [11] or a channel-drop filter [15]. The third example involves a metamaterial unit element consisting of an infinitely long isolated cylindrical dielectric rod [19].

In each of the three representative examples, one design feature is assumed to have some inherent uncertainty. The uncertain model parameter is either a dimension or a material property. Since these structures are nano-fabricated, it is common to have uncertainties in feature dimensions. Similarly, since

the desired material properties of some of these nano-fabricated structures are achieved using doping, uncertainties in the material properties are also likely. The uncertainty in the performance of each device is quantified using a statistical description of an "output" field quantity for a given uncertainty in the "input" or model parameter. The variations in the chosen output quantity for these three different representative examples are observed to be very dissimilar both in terms of type and magnitude of variation.

The efficiency of uncertainty quantification is evaluated for four different sampling methods in each of the three representative examples. The accuracy of the estimated mean and standard deviation of the output quantity is computed as a function of the number of samples for deterministically and randomly chosen samples using either a uniform distribution or the distribution of the uncertain parameter. A comparison of efficiency across different sampling methods reveals that uniform deterministic sampling method provides the most efficient uncertainty quantification in each case studied. Analysis of the results suggests that uniform deterministic sampling is the best sampling strategy in the absence of strong prior information on how the output varies with the uncertain parameter.

The three representative examples are described in detail in Section 5.2. The analysis methods used for the investigation of the efficiency of the sampling methods are also described in Section 5.2. The results from the investigation of the efficiency of the sampling methods for the three representative examples are presented and discussed in Section 5.3. Concluding remarks are provided in Section 5.4.

5.2 Test beds and Analysis Methods

5.2.1 Waveguide branch

A 90° waveguide branch is a common building block in photonic crystal circuits (e.g. [11]–[14]). A schematic diagram of the 2D photonic crystal waveguide branch used as a testbed for this study is shown in Figure 5.1(a). The specific configuration for this waveguide branch is taken from [11]. The black circles represent cross sections of cylindrical silicon rods (ϵ_r = 11.56), each of which is surrounded by air. The rods form a periodic array with a lattice constant of a. The radius of each rod is $0.2a$. The line of missing rods in the array serves as a waveguide that permits the transmission of a TM_z wave (where z is perpendicular to the plane of the array) from the input channel to the output channels of the device. The frequency of operation is chosen to be $0.35(c/a)$, where c is the speed of light in air.

The radius of the center rod (in red) of the waveguide branch is chosen as the model parameter that has statistical uncertainty. The mean radius of the center rod is $0.2a$, and its probability density is described by a beta (3, 3) distribution as shown in Figure 5.2(a) [3]. This distribution for the rod radius has finite support between 50% and 150% of the mean value of the radius. The transmissivity of the waveguide branch, defined as the fraction of the incident power at the input channel that exits through the output

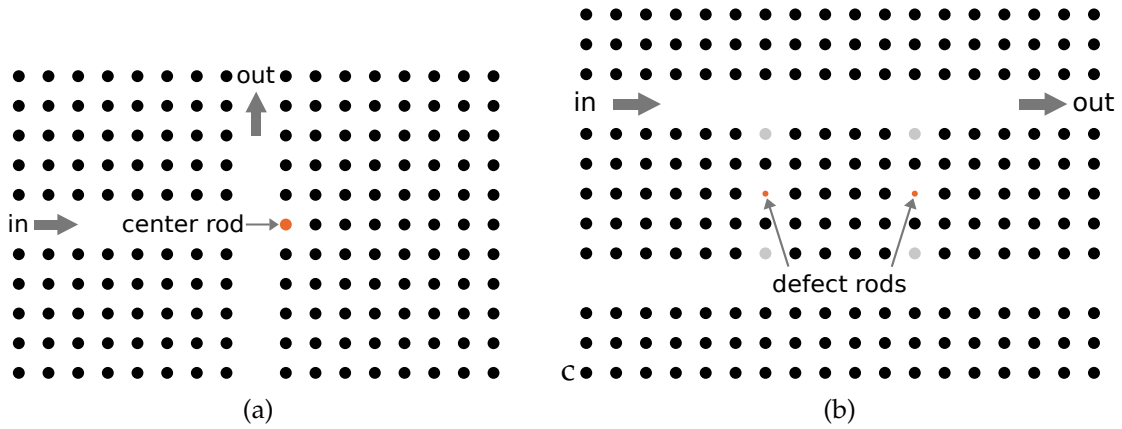

Figure 5.1: Schematic diagrams for two 2-D photonic crystal waveguide devices comprising arrays of cylindrical silicon rods (black) surrounded by air. (a) Waveguide branch with uncertainty in the radius of the center rod (red). (b) Channel-drop filter with uncertainty in the permittivity of the defect rods (red).

channel, as labeled in Figure 5.1(a), is normalized by its maximum possible value of 0.5. This normalized transmissivity is chosen as the output field quantity of interest for which the mean and standard deviation are to be estimated.

5.2.2 Channel-drop filter

Channel-drop filters represent another canonical class of photonic-crystal-based devices used in photonic integrated circuits (e.g. [15]–[18]). The schematic diagram of the 2D photonic crystal channel-drop filter used as the second testbed for our study is shown in Figure 5.1(b). This specific configuration was reported in [15]. The black, grey, and red circles represent cross sections of cylindrical rods. The black circles that comprise the vast majority of elements in the photonic crystal correspond to silicon rods (ϵ_r=11.56), each with a radius of $0.2a$. The four grey circles near the center of the diagram represent coupling rods that have the same radius as the silicon rods but a different permittivity (ϵ_r = 9.5). The two smaller red circles at the center represent the defect rods each with a radius of $0.05a$. The coupling and defect rods assist in coupling the light from the "add" waveguide near the top of the diagram to the "drop" waveguide near the bottom of the diagram. The frequency of operation is chosen to be $0.37306(c/a)$. This corresponds to the filter's drop frequency, that is, the frequency at which the light entering the device through the input port of the add waveguide is almost entirely coupled to the adjacent drop waveguide leaving very little light to exit through the add waveguide's output port. The transmissivity at this frequency is highly sensitive to the defect rod permittivity.

The relative permittivity of the defect rods is chosen as the model parameter that has uncertainty. The mean value is ϵ_r = 6.6. A normal distribution is assumed for the permittivity's probability density function

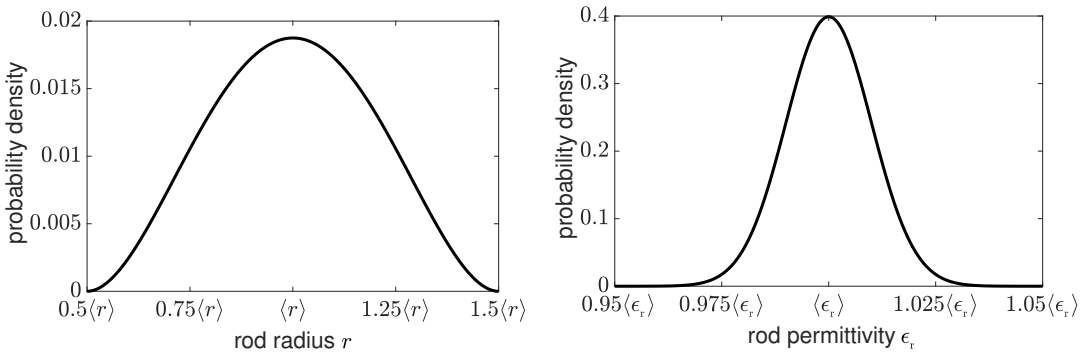

Figure 5.2: Probability density functions for the rod radius and permittivity in three simulated structures. $\langle\cdot\rangle$ represents mean value. (a) Beta (3, 3) distribution representing the radius of the center rod in the waveguide branch and the radius of the isolated rod. (b) Normal distribution representing the permittivity of the defect rods in the channel-drop filter.

as shown in Figure 5.2(b). The standard deviation for this distribution is 1% of the mean value. Since the normal distribution does not have finite support, we confine the permittivity sample space to a range spanning 95% and 105% of the mean value; this corresponds to a width of 10 standard deviations – a range that is sufficiently wide to permit truncating the distribution outside of this range. The transmissivity of the channel-drop filter, defined as the fraction of the incident power that exits the device through the output port, as labeled in Figure 5.1(b), is chosen as the output field quantity of interest for this testbed.

5.2.3 Isolated dielectric rod

The polarizability of a single infinitely long cylindrical dielectric rod in air [19] exhibits resonances that give rise to exotic properties of all-dielectric metamaterials consisting of numerous such rods embedded in a background medium. We specifically take the example of a TM_z-polarized plane wave incident on a z-oriented infinitely long cylindrical rod of $\epsilon_r = 18$ [19] as the third testbed in this study.

The radius of the rod is chosen as the parameter that has uncertainty. The mean value of the radius is $0.2\lambda_0$ where λ_0 is the free-space wavelength corresponding to the chosen frequency of operation. The probability density of the uncertain radius is assumed to be a beta (3, 3) distribution as shown in Figure 5.2(a) [3]. This distribution has finite support between 50% and 150% of the mean value. The polarizability of the rod in the z-direction (α_{zz}) normalized by the cross-sectional area of the dielectric rod, is the chosen output field quantity of interest for this testbed.

5.2.4 Analysis methods

The normalized transmissivity as a function of the center rod radius in the waveguide branch example, the normalized transmissivity as a function of the defect rod permittivity in the channel-drop filter example, and the normalized polarizability as a function of the rod radius in the isolated rod example are plotted in Figures 5.3(a), (b), and (c), respectively. These plots illustrate the characteristics of the output quantity. The plots in Figures 5.3(a) and (b) were obtained by conducting CEM simulations of the waveguide branch and the channel-drop filter respectively for 500,000 different values of the corresponding uncertain parameter uniformly distributed over the sample space. The CEM simulations were conducted using the finite-difference time-domain (FDTD) [20] technique. The plot in Figure 5.3(c) was obtained by evaluating the known analytical solution [21] for normalized polarizability at 500,000 different values of the corresponding uncertain parameter, uniformly distributed over the full range of its sample space.

The mean and standard deviation were estimated using deterministic or randomly chosen samples obtained using both a uniform distribution and the probability distribution of the uncertain parameter. The output quantities were obtained using CEM simulations in the case of waveguide branch and channel-drop filter and the known analytical solution in the case of the isolated rod. The output as a function of the uncertain parameter was approximated using spline interpolation[1]. The mean and variance integrands of the output for each example were estimated using the spline fit and the probability distribution of the uncertain input parameter. The actual mean and variance integrands were similarly obtained using the dense samplings depicted in Figure 5.3. The performance of random sampling methods is characterized using the median and upper/lower quartiles of 1000 sets of samples.

5.3 Results and Discussion

The unique features observed in each of the three plots in Figure 5.3 indicate that the three examples used for the investigation in this paper are distinct in nature. The impact of sampling is illustrated in Figure 5.4 by comparing the true integrand for the variance to the spline fit based on seven deterministically chosen samples. Both uniformly distributed samples and samples chosen based on the distribution of the uncertain parameter are shown for all three devices.

Figure 5.4(a) shows that the spline fit based on uniform sampling underestimates the area under the transmissivity variance integrand curve between $1.2\langle r\rangle$ and $1.35\langle r\rangle$ and overestimates the area between $1.35\langle r\rangle$ and $1.5\langle r\rangle$. The overestimation and underestimation errors tend to offset each other. The spline fit based on beta (3, 3) sampling overestimates the area under the transmissivity variance integrand curve

[1]Other interpolation/function-fitting techniques were investigated ([6]–[10], [22]) but no significant improvements over spline interpolation were observed in terms of the efficiency of uncertainty quantification.

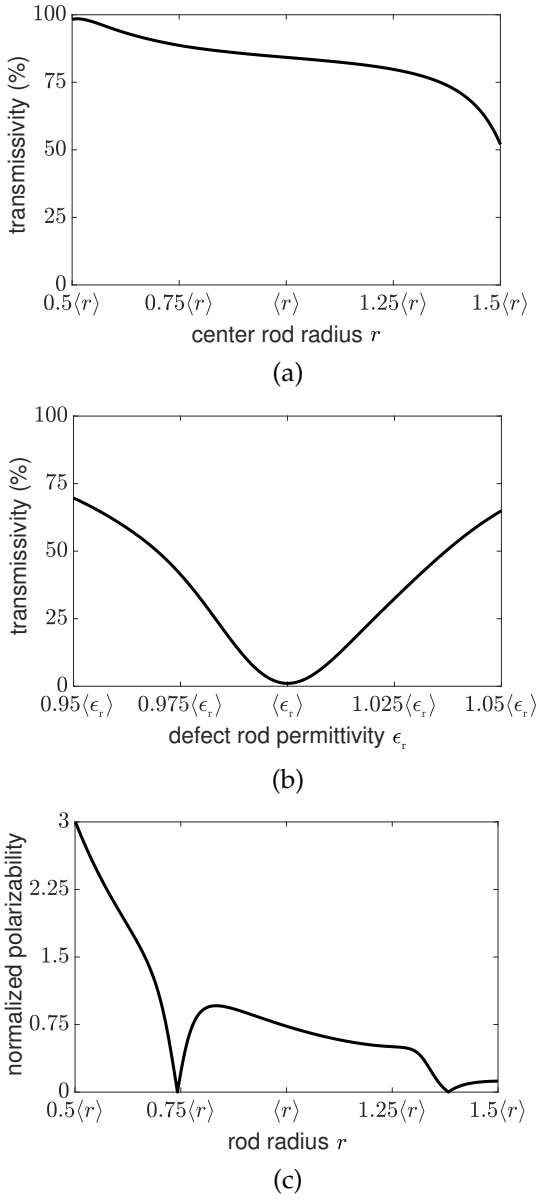

Figure 5.3: Computed device performance characteristics as functions of rod radius and permittivity. $\langle\cdot\rangle$ represents mean value. (a) Transmissivity of the waveguide branch, normalized by its maximum possible value (50%). (b) Transmissivity of the channel-drop filter. (c) Polarizability of the isolated rod, normalized by the rod's cross-sectional area.

between $1.25\langle r\rangle$ and $1.5\langle r\rangle$. This is due to the fact that the beta (3, 3) distributed samples are concentrated in the central region between $0.8\langle r\rangle$ and $1.2\langle r\rangle$. In this example, the spline fit based on the uniformly distributed samples approximates the transmissivity variance integrand function better than one based on

beta (3, 3) distributed samples because the samples outside the central region lead to a better approximation of the integrand.

In Figure 5.4(b), the spline fit based on uniform sampling is nearly indistinguishable from the actual transmissivity variance integrand curve. The transmissivity function is a very smooth curve as seen in Figure 5.3(b). A low quality factor trough is present at the mean value of uncertain parameter. Consequently, the transmissivity variance integrand function is also very smooth as seen in the black reference plot in Figure 5.4(b). This very smooth curve can be very accurately approximated using a spline fit based on a small number of uniformly distributed samples. However, the spline fit based on normally distributed samples overestimates the area under the transmissivity variance integrand curve outside the central region of $0.985\langle\epsilon_r\rangle$ to $1.015\langle\epsilon_r\rangle$. This is due to the fact that the samples are concentrated in the central region of $0.985\langle\epsilon_r\rangle$ to $1.015\langle\epsilon_r\rangle$. Lack of samples results in poor accuracy outside this region. Uniform sampling provides a more accurate fit to the variance integrand than normal sampling, leading to more accurate variance estimates.

Neither uniform nor beta (3, 3) distributed samples capture the sharp features that are present in the actual polarizability variance integrand shown in Figure 5.4(c) due to an insufficient number of samples. An increase in the number of samples is expected to significantly improve the accuracy of the spline fits. A small increase in the number of samples will lead to the new samples populating the region given by $r < 0.8\langle r\rangle$ and thereby dramatically improving the accuracy of spline fits. The accuracy is expected to improve faster with uniform sampling because it leads to proportionally more samples throughout the region $0.5\langle r\rangle$ to $0.8\langle r\rangle$. In contrast, beta (3, 3) sampling concentrates samples near $\langle r\rangle$.

These three examples illustrate that important features in the variance integrand are not generally located in the high probability regions of the uncertain parameter. Hence, uniform sampling is more likely to capture these features and produce more accurate results. This inference is supported by the numerical evaluation of the mean and standard deviation that follows.

The accuracy of the estimated mean or standard deviation based on random sampling varies considerably as shown by the large inter-quartile range in each of the Figures 5.5, 5.6, and 5.7. This uncertainty in the error is a significant disadvantage of random sampling.

The median errors of random sampling are comparable to deterministic sampling using the probability distribution of the uncertain parameter for the waveguide branch (Figures 5.5(a)-(b)) and channel-drop filter (Figures 5.6(a)-(b)). In contrast, uniform deterministic sampling generally outperforms more that 75% of uniformly generated random sampling realizations for these two examples (Figures 5.5(c)-(d); Figures 5.6(c)-(d)). Uniform deterministic sampling also is observed to outperform both random sampling strategies and deterministic sampling based on the distribution of the uncertain parameter in Figures 5.5 and 5.6.

These results are consistent with the nature of the spline fits observed in Figures 5.4(a)-(b). Uniform deterministic sampling better captures the behavior of the integrand over the range of the uncertain parameter.

The results for the isolated rod polarizability shown in Figure 5.7 are consistent with those of waveguide branch and channel-drop filter provided the complex features present in Figure 5.3(c) are considered. For example the performance of all the deterministic sampling approaches is a non-monotone function of the number of samples. Changing the number of deterministic samples also changes the location of those samples. The effect of sample location is significant when the number of samples is relatively small due to the complexity of relationship between rod radius and polarizability. Random sampling schemes have identical limitations; the median and inter-quartile ranges are only monotone decreasing because they are averaged over many realizations. Note that deterministic sampling has generally better performance than the median of random sampling for more than 45 beta (3, 3) samples or more than 10 uniform samples.

As with the waveguide branch and channel-drop filter, uniform deterministic sampling (Figures 5.7(c)-(d)) outperforms deterministic sampling based on the probability distribution of the uncertain rod radius (Figures 5.7(a)-(b)). Furthermore, Figure 5.7 indicates that uniform deterministic sampling outperforms a majority of the realizations obtained by random sampling.

The deterministic sampling errors are also non monotone functions of the number of samples in the channel-drop filter as shown in Figure 5.6. The degree of non-monotonicity in the channel-drop filter is much less than that of the rod polarizability shown in Figure 5.7 because the quality factor of the null in transmissivity is much lower than the quality factors of nulls in normalized polarizability. Higher quality factors increase the sensitivity of the results to the exact locations of samples.

In general, it is impossible to predict in advance the regions of the sample space containing the most important features of the output function for estimating its moments. Furthermore, as illustrated in these three test beds, the regions of sample space containing important features do not correspond to high probability regions of the uncertain parameter. These attributes favor a uniform deterministic sampling strategy as it is less likely to undersample important features in the output function. Indeed, the best overall accuracy is obtained using uniform deterministic sampling in all three examples studied in this paper. Improving on uniform deterministic sampling requires either *a priori* information concerning the dependence of the output function on the uncertain parameters or being lucky when choosing samples randomly.

5.4 Conclusion

This investigation has demonstrated two key points. The first point is that the uniform deterministic sampling strategy has a significant advantage over other deterministic or random sampling strategies in terms of the efficiency of uncertainty quantification in three distinct representative examples namely

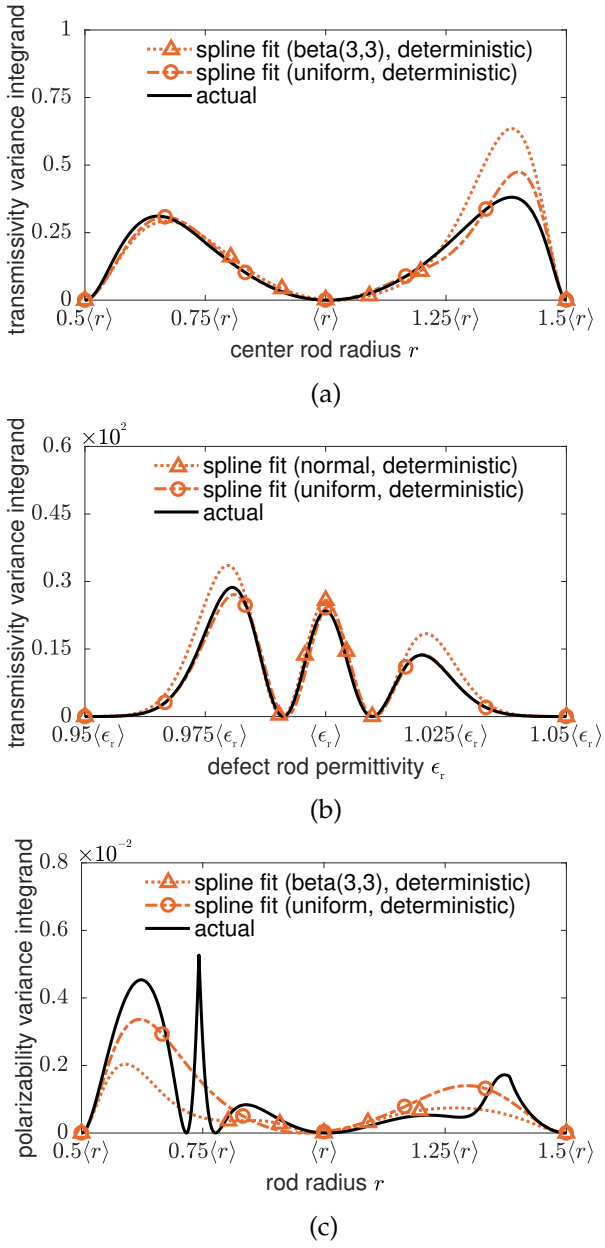

Figure 5.4: Computed variance integrands for device performance characteristics as functions of rod radius and permittivity. The actual integrand (black solid line) is compared with spline fits (red dotted and dashed lines) obtained using function evaluations at seven sample values (circles/triangles). Samples are deterministically chosen and are either uniformly distributed or have the same distribution as that of the design parameter. $\langle\cdot\rangle$ represents mean value. (a) Transmissivity of the waveguide branch. (b) Transmissivity of the channel-drop filter. (c) Polarizability of the isolated rod.

waveguide branch, channel-drop filter, and isolated photonic crystal rod. The second point is that improving over uniform deterministic sampling in terms of efficiency requires *a priori* information concerning the

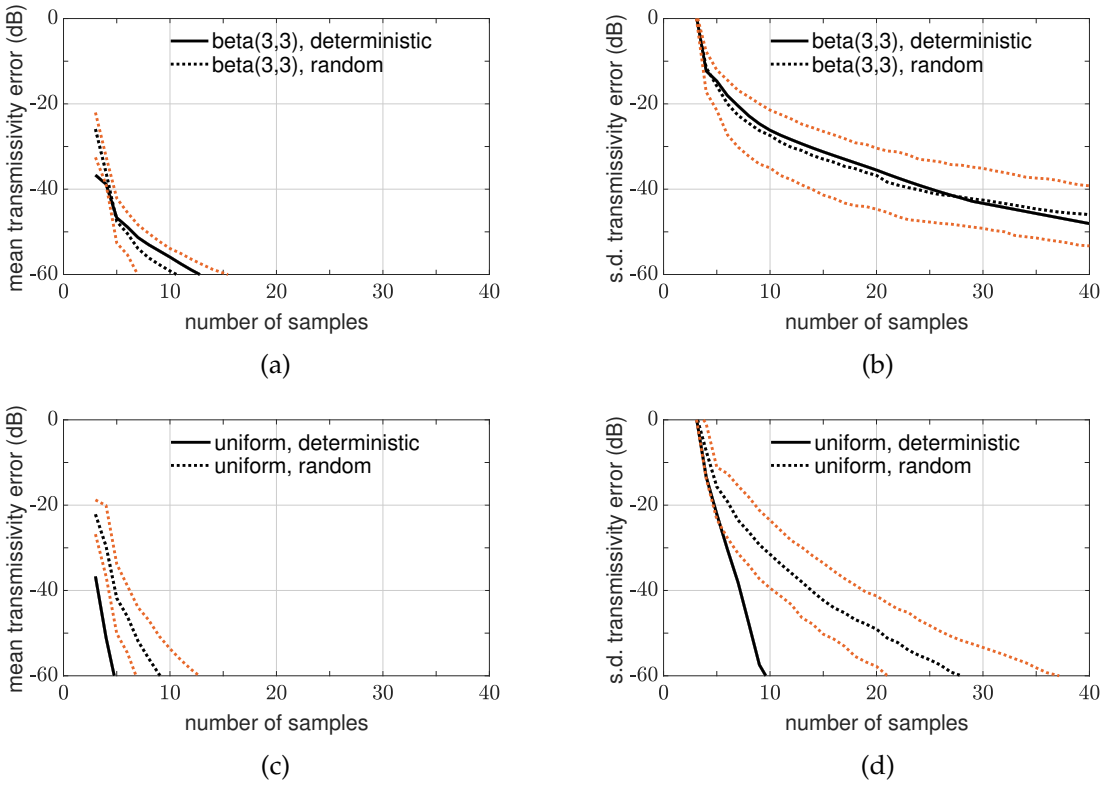

Figure 5.5: Errors (dB) in the estimated mean and standard deviation (s.d.) of the waveguide branch transmissivity as a function of the number of samples used in the spline fits. Both deterministic and random sampling techniques are considered. Random sampling errors are quantified in terms of the median (black dotted line) as well as upper and lower quartiles (red dotted lines) for 1000 random realizations. (a) Error estimating mean, beta (3, 3) sampling. (b) Error estimating the standard deviation, beta (3, 3) sampling. (c) Error estimating mean, uniform sampling. (d) Error estimating the standard deviation, uniform sampling.

dependence of the output function on the uncertain parameters which is not possible to obtain in case of realistic uncertainty quantification problems.

Deterministic sampling is seen to be advantageous in terms of reliable efficiency of uncertainty quantification in favor of random sampling for all the three distinct representative examples investigated. This is based on the fact that the large interquartile ranges seen in the figures for random sampling demonstrates the range of variation in the accuracy of uncertainty quantification with varying sampling realizations. Even when the deterministic sampling strategy produces a non-monotone functions of errors in mean and standard deviation with respect to number of samples, as in the example of isolated rod, the disadvantage is not limited to deterministic sampling but also extends to any sampling realization of random sampling.

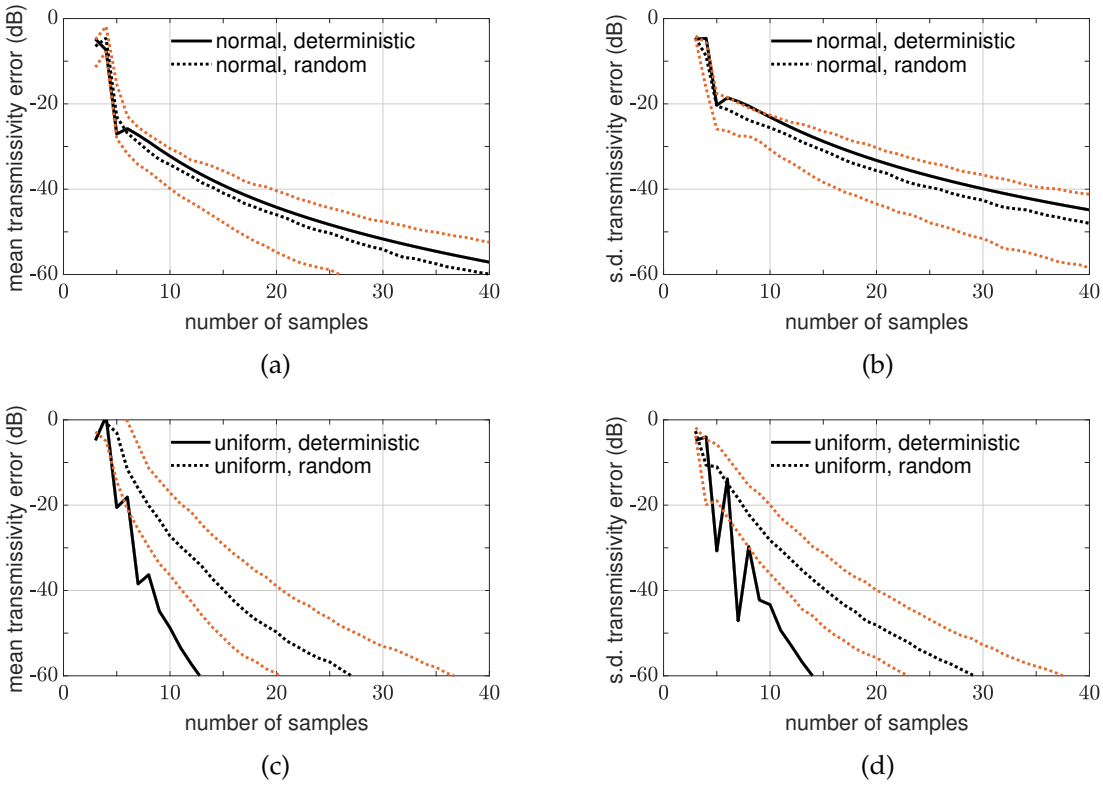

Figure 5.6: Errors (dB) in the estimated mean and standard deviation (s.d.) of the channel-drop filter transmissivity as a function of the number of samples used in the spline fits. Both deterministic and random sampling techniques are considered. Random sampling errors are quantified in terms of the median (black dotted line) as well as upper and lower quartiles (red dotted lines) for 1000 random realizations. (a) Error estimating mean, normal sampling. (b) Error estimating the standard deviation, normal sampling. (c) Error estimating mean, uniform sampling. (d) Error estimating the standard deviation, uniform sampling.

The investigation can be extended to include adaptive sampling techniques as future work in order to see how advantageous it is, if at all, to use adaptive sampling over uniform deterministic sampling for the same three representative examples.

5.5 References

[1] R. Y. Rubinstein and D. P. Kroese, *Simulation and the Monte Carlo Method*, 3rd ed., Hoboken, NJ, USA: Wiley, 2017.

[2] R. S. Edwards, A. C. Marvin, and S. J. Porter, "Uncertainty analyses in the finite-difference time-domain method," *IEEE Trans. Electromagn. Compat.*, **52**, 1, pp. 155–163, 2010.

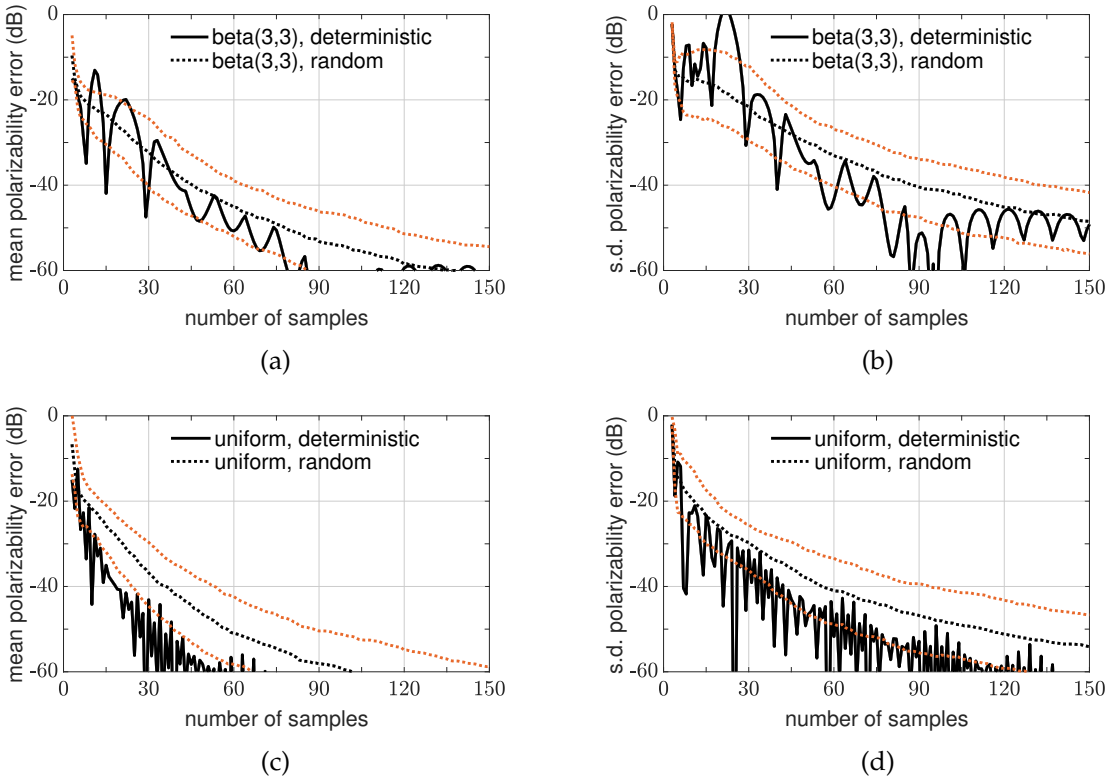

Figure 5.7: Errors (dB) in the estimated mean and standard deviation (s.d.) of the isolated rod polarizability as a function of the number of samples used in the spline fits. Both deterministic and random sampling techniques are considered. Random sampling errors are quantified in terms of the median (black dotted line) as well as upper and lower quartiles (red dotted lines) for 1000 random realizations. (a) Error estimating mean, beta (3, 3) sampling. (b) Error estimating the standard deviation, beta (3, 3) sampling. (c) Error estimating mean, uniform sampling. (d) Error estimating the standard deviation, uniform sampling.

[3] A. C. M. Austin and C. D. Sarris, "Efficient analysis of geometrical uncertainty in the FDTD method using polynomial chaos with application to microwave circuits," *IEEE Trans. Microw. Theory Tech.*, **61**, 12, pp. 4293–4301, 2013.

[4] S. M. Smith and C. Furse, "Stochastic finite-difference time-domain (FDTD) for analysis of statistical variation in electromagnetic fields," *IEEE Trans. Antennas Propag.*, **60**, 7, pp. 3343–3350, 2012.

[5] M. L. Gilbert and F. L. Teixeira, "A small-perturbation automatic-differentiation method for determining uncertainty in computational electromagnetics," *IEEE Trans. Antennas Propag.*, **60**, 11, pp. 5305–5314, 2012.

[6] N. Kovvali, *Theory and Applications of Gaussian Quadrature Methods*, 1st ed., San Rafael, CA, USA: Morgan & Claypool, 2011.

[7] C. Chauviere, J. S. Hesthaven, and L. Lurati, "Computational modeling of uncertainty in time-domainn electromagnetics," *SIAM J. Sci. Comput.*, **28**, 2, pp. 751–755, 2006.

[8] A. C. Yücel, H. Bagcı, and E. Michielssen, "An adaptive multi-element probabilistic collocation method for statistical EMC/EMI characterization," *IEEE Trans. Electromagn. Compat.*, **55**, 6, pp. 1154–1168, 2013.

[9] Z. Zhang, T.-W. Weng, and L. Daniel, "Big-data tensor recovery for high-dimensional uncertainty quantification of process variations," *IEEE Trans. Compon., Packag., Manuf. Technol.*, **7**, 5, pp. 687–697, 2017.

[10] A. C. M. Austin, N. Sood, J. Siu, and C. D. Sarris, "Application of polynomial chaos to quantify uncertainty in deterministic channel models," *IEEE Trans. Antennas Propag.*, **61**, 11, pp. 5754–5761, 2013.

[11] S. Fan, S. G. Johnson, J. D. Joannopoulos, C. Manolatou, and H. A. Haus, "Waveguide branches in photonic crystals," *J. Opt. Soc. Am. B*, **18**, 2, pp. 162–165, 2001.

[12] B. Chen, L. Huang, C. Liu, Y. Li, and G. Liu, "A simple broadband T-shaped waveguide branch in photonic crystals," *Opt. Commun.*, **285**, 1, pp. 41–45 , 2012.

[13] E. Bulgakov and A. Sadreev, "Symmetry breaking in a T-shaped photonic waveguide coupled with two identical nonlinear cavities," *Phys. Rev. B*, **84**, 155304, 2011.

[14] E. H. Shaik and N. Rangaswamy, "Improved design of all-optical photonic crystal logic gates using T-shaped waveguide," *Opt. Quantum Electron.*, **48**, 1, pp. 1-15, 2016.

[15] S. Fan, P. R. Villeneuve, J. D. Joannopoulos, and H. A. Haus, "Channel-drop filters in photonic crystals," *Opt. Express*, **3**, 1, pp. 4–11, 1998.

[16] H. Ren, C. Jiang, W. Hu, M. Gao, and J. Wang, "Photonic crystal channel drop filter with a wavelength-selective reflection micro-cavity,", *Opt. Express*, **14**, 6, pp. 2446–2458, 2006.

[17] L. Li and G. Q. Liu, "Photonic crystal ring resonator channel drop filter," *Optik*, **124**, 17, pp. 2966–2968, 2013.

[18] A. Dideban, H. Habibiyan, and H. Ghafoorifard, "Photonic crystal channel drop filters based on circular-shaped cavities," *Photon Netw. Commun.*, **34**, 3, pp. 468–477, 2017.

[19] E. Kallos, I. Chremmos, and V. Yannopapas, "Resonance properties of optical all-dielectric metamaterials using two-dimensional multipole expansion," *Phys. Rev. B*, **86**, 245108, 2012.

[20] A. Taflove and S. C. Hagness, *Computational Electrodynamics: The Finite-Difference Time-Domain Method*, 3rd ed., Norwood, MA, USA: Artech House, 2005.

[21] K. Vynck, D. Felbacq, E. Centeno, A. I. Căbuz, D. Cassagne, and B. Guizal, "All-dielectric rod-type metamaterials at optical frequencies," *Phys. Rev. Lett.*, **102**, 133901, 2009.

[22] A. Kaintura, D. Spina, I. Couckuyt, L. Knockaert, W. Bogaerts, and T. Dhaene, "A kriging and stochastic collocation ensemble for uncertainty quantification in engineering applications," *Engineering with Computers*, **33**, 4, pp. 935–949, 2017.